Spectral models for low-luminosity active galactic nuclei in LINERs: the role of advection-dominated accretion and jets

Rodrigo S. Nemmen,[1]★ Thaisa Storchi-Bergmann[2] and Michael Eracleous[3]

[1]*NASA Goddard Space Flight Center, Greenbelt, MD 20771, USA*
[2]*Instituto de Física, Universidade Federal do Rio Grande do Sul, Campus do Vale, Porto Alegre, RS, Brazil*
[3]*Department of Astronomy and Astrophysics, Pennsylvania State University, 525 Davey Lab, University Park, PA 16802, USA*

ABSTRACT

We perform an exploratory study of the physical properties of accretion flows and jets in low-luminosity active galactic nuclei (LLAGNs) by modelling the spectral energy distributions (SEDs) of 12 LLAGNs in low-ionization nuclear emission-line regions (LINERS). These SEDs we constructed from high-resolution radio, X-ray and optical/ultraviolet (UV) observations of the immediate vicinity of the black hole. We adopt a coupled accretion-jet model comprising an inner advection-dominated accretion flow (ADAF) and an outer standard thin disc. We present best-fitting models in which either the ADAF or the jet dominates the X-ray emission. Six sources in our sample display an optical–UV excess with respect to ADAF and jet models; this excess can be explained as emission from the truncated disc with transition radii 30–225 R_S in four of them. In almost all sources the optical emission can also be attributed to unresolved, old stellar clusters with masses $\sim 10^7$–10^8 M$_\odot$. We find evidence for a correlation between the accretion rate and jet power and an anticorrelation between the radio loudness and the accretion rate. We confirm previous findings that the radio emission is severely underpredicted by ADAF models and explained by the relativistic jet. We find evidence for a non-linear relation between the X-ray and bolometric luminosities and a slight IR excess in the average model SED compared to that of quasars. We suggest that the hardness of the X-ray spectrum can be used to identify the X-ray emission mechanism and discuss directions for progress in understanding the origin of the X-rays.

Key words: accretion, accretion discs – black hole physics – galaxies: active – galaxies: jets – galaxies: nuclei – galaxies: Seyfert.

1 INTRODUCTION

In the present-day universe, supermassive black holes (SMBHs) are underfed compared to the ones at high redshifts and are 'sleeping'. Most of SMBH activity at low z is dominated by the weak end of the active galactic nucleus (AGN) luminosity function in the form of low-luminosity AGNs (LLAGNs; Ho, Filippenko & Sargent 1995, 1997b; Nagar, Falcke & Wilson 2005; Ho 2008). LLAGNs are extremely sub-Eddington systems which are many orders of magnitude less luminous than quasars, with average bolometric luminosities $L_{\rm bol} \lesssim 10^{42}$ erg s^{-1} and an average Eddington ratio of $L_{\rm bol}/L_{\rm Edd} \sim 10^{-5}$ (Ho 2009) where $L_{\rm Edd}$ is the Eddington luminosity. Though the LLAGN phase dominates the time evolution of SMBHs, it contributes little to their mass growth (Hopkins & Hernquist 2006; Sijacki et al. 2007; Merloni & Heinz 2008; Xu & Cao 2010). The

bulk of the LLAGN population ($\approx 2/3$; Ho 2008, 2009) reside in low-ionization nuclear emission-line regions (LINERs; Heckman 1980; Ho, Filippenko & Sargent 1997a).

The observational properties of LLAGNs are quite different from those of more luminous AGNs. Regarding the broad-band spectral energy distributions (SEDs), LLAGNs do not seem to have the thermal continuum prominence in the ultraviolet (UV) – the 'big blue bump' – which is one of the signatures of the presence of an optically thick, geometrically thin accretion disc (Ho 1999, 2008; Nemmen et al. 2006; Wu, Yuan & Cao 2007; Eracleous, Hwang & Flohic 2010a). Regarding the emission lines, LLAGNs typically have weak and narrow Fe Kα emission (Terashima et al. 2002) and a handful of LINERs display broad double-peaked Hα lines (e.g. Storchi-Bergmann et al. 2003); these properties of the emission-line spectrum are consistent with the absence of a thin accretion disc, or a thin accretion disc whose inner radius is truncated at $\gtrsim 100 GM/c^2$ (Chen & Halpern 1989; Chen, Halpern & Filippenko 1989). Last but not least, with the typical gas supply available via ordinary

★ E-mail: rodrigo.nemmen@nasa.gov

mass-loss from evolved stars and gravitational capture of gas from the hot interstellar medium (i.e. Bondi accretion) in nearby galaxies, LLAGNs would be expected to produce much higher luminosities than observed on the assumption of standard thin discs with a 10 per cent radiative efficiency (Soria et al. 2006b; Ho 2009). Taken together, this set of observational properties favours the scenario in which the accretion flow in LLAGNs is advection dominated or radiatively inefficient.

Advection-dominated accretion flows (ADAFs;[1] for reviews, see Narayan, Mahadevan & Quataert 1998; Yuan 2007; Narayan & Mc-Clintock 2008) are very hot, geometrically thick, optically thin flows which are typified by low radiative efficiencies ($L \ll 0.1\dot{M}c^2$) and occur at low accretion rates ($\dot{M} \lesssim 0.01\dot{M}_{\text{Edd}}$). SMBHs are thought to spend most of their lives in the ADAF state (Hopkins, Narayan & Hernquist 2006; Xu & Cao 2010), the best studied individual case being Sgr A* (e.g. Yuan 2007).

In many LLAGNs, another component in the accretion flow besides the ADAF is required in order to account for a number of observations, including a prominence in the mid- or near-IR and steep fall-off of the spectrum in the optical–UV (OUV) region – a 'red bump' (Lasota et al. 1996; Quataert et al. 1999; Nemmen et al. 2006; Ho 2008; Yu et al. 2011; Wu, Yan & Yi 2013) – as well as the presence of double-peaked Balmer emission lines (e.g. Storchi-Bergmann et al. 2003; Eracleous, Lewis & Flohic 2009): the emission from a thin accretion disc whose inner radius is truncated at the outer radius of the ADAF. The accretion flow may begin as a standard thin disc but somehow at a certain transition radius it gradually switches from a cold to a hot ADAF mode. The details of how this transition might happen are still not well understood (Manmoto et al. 2000; Yuan & Narayan 2004; Narayan & McClintock 2008), but it seems to be analogous to the transition between the different spectral states in black hole binary systems (Remillard & McClintock 2006; Done, Gierliński & Kubota 2007).

Maoz (2007) challenged the scenario of the central engines of LLAGNs consisting of ADAFs and truncated thin discs. Maoz argues that LLAGNs in LINERs have UV/X-ray luminosity ratios similar on average to those of brighter Seyfert 1s, and based on that observation he posits that thin discs extending all the way down to the radius of the innermost stable circular orbits persist even for LLAGNs, despite their smaller accretion rates. Yu et al. (2011) showed that the SEDs compiled by Maoz (2007) are naturally fitted by ADAF models with the addition of a truncated thin disc and also discussed on theoretical grounds why the ADAF model has a superior explanation capability than the pure thin disc model. The ADAF model is the only model that can naturally account for the set of observational properties of LLAGNs within a self-contained theoretical framework. Hence, it is the physical scenario adopted in this work.

ADAFs are relevant to the understanding of AGN feedback since they are quite efficient at producing powerful outflows and jets, as suggested by theoretical studies including analytical theory (Narayan & Yi 1994; Nemmen et al. 2007; Begelman 2012) and numerical simulations (McKinney & Gammie 2004; Hawley & Krolik 2006; Tchekhovskoy, Narayan & McKinney 2011; McKinney, Tchekhovskoy & Blandford 2012; Yuan, Bu & Wu 2012). This is in line with the different observational studies that demonstrate that LLAGNs are generally radio loud (Nagar et al. 2000; Nagar, Wilson & Falcke 2001; Ho 2002, 2008; Younes et al. 2012) and ac-

companied by powerful jets (e.g. Heinz, Merloni & Schwab 2007; Merloni & Heinz 2008).

It is clear then that an understanding of the physical nature of LLAGNs in LINERs will shed light on the nature of black hole accretion, outflows and consequently black hole growth and AGN feedback in present-day galaxies. One of the best ways of exploring the astrophysics of black hole accretion and outflows is by using multiwavelength observations of black hole systems and comparing the spectra predicted by specific models with the data. The goal of this work is therefore to probe the physics of accretion and ejection in the LLAGN population, by carrying out an exploratory modelling of their nuclear, broad-band, radio-to-X-ray SEDs which provide constraints on physical models for the emission of the accretion flow and the jet. Furthermore, with a large enough sample of systems, we can derive from the fits to the data the parameters that characterize the central engines and build a census of the 'astrophysical diet' of low-state AGNs.

The structure of this paper is as follows. In Section 2, we describe the sample of 21 LLAGNs in LINERs that we used, the data and the criteria that we use to select the 12 best sampled SEDs. Section 3 describes the physical model that we adopted in order to interpret and fit the SEDs and derive the central engine parameters. In Section 4, we describe the model fits to the SEDs. In Section 5, we describe the parameters resulting from our model fits and possible correlations between accretion and jet production. We present the average SED resulting from our fits in Section 6, including the predicted emission in wavebands which can be observed with future facilities such as the Atacama Large Millimeter/submillimeter Array. We discuss the role of the ADAF and jet in explaining the X-ray emission, the constraints on the transition radius and the limitations of our models in Section 7, outlining along the way the directions for progress on these issues. We conclude by presenting a summary of our results in Section 8. In Appendices A and B, we discuss the uncertainties in the model parameters that we derive and present illustrative model fits to the nine sparsely sampled SEDs which were left out of the main analysis.

2 SAMPLE

Eracleous et al. (2010a, hereafter EHF10) compiled a sample of 35 SEDs of LLAGNs found in LINERs which include high spatial resolution optical and UV observations with the *Hubble Space Telescope* (*HST*), as well as X-ray observations with *Chandra* and high-resolution radio observations with the Very Large Array (VLA) or Very Long Baseline Array/very long baseline interferometry.

LINERs constitute quite a heterogeneous class of objects. For instance, their nature and particularly the nature of the source of power for their line emission has been repeatedly questioned (e.g. Eracleous, Hwang & Flohic 2010b; Sarzi et al. 2010; Yan & Blanton 2012; Singh et al. 2013). For example, Yan & Blanton (2012) concluded that the line emission observed in large-aperture (>100 pc) spectroscopy in most of the LINER-like galaxies in their sample is not primarily powered by an accreting black hole and thus urge caution in associating the corresponding line emission with the AGN bolometric luminosity. Therefore, in order to select from the sample of EHF10 the sources for which the nuclear emission is most probably associated with black hole accretion – thus providing the best SEDs to be compared against accretion flow and jet models – we carefully applied the following selection criteria.

(1) Availability of black hole mass estimates. We limited ourselves only to galaxies with black hole mass estimates since the

---

[1] In this paper, we consider ADAFs and radiatively inefficient accretion flows to be the same kind of accretion flow solution. For a clarification regarding the terminology, see Yu, Yuan & Ho (2011).

Table 1. Sample of galaxies and their basic properties. The information in this table was obtained from EHF10, see the text.

Galaxy	Hubble type	Distance[a] (Mpc)	log $(M_{BH}/M_{\odot})$	LINER type	L_X (erg s^{-1})[b]	L_{bol} (erg s^{-1})[c]	L_{bol}/L_{Edd}
NGC 1097	SB(rl)b	14.5 (1)	8.1	L1	4.3×10^{40}	8.5×10^{41}	5×10^{-5}
NGC 3031 (M81)	SA(s)ab	3.6 (3)	7.8	S1.5/L1	1.9×10^{40}	2.1×10^{41}	3×10^{-5}
NGC 3998	SA(r)0	13.1 (2)	8.9	L1	2.6×10^{41}	1.4×10^{43}	1×10^{-4}
NGC 4143	SAB(s)0	14.8 (2)	8.3	L1	1.1×10^{40}	3.2×10^{41}	1×10^{-5}
NGC 4261	E2-3	31.6 (2)	8.7	L2	1.0×10^{41}	6.8×10^{41}	1×10^{-5}
NGC 4278	E1-2	14.9 (2)	8.6	L1	9.1×10^{39}	2.7×10^{41}	5×10^{-6}
NGC 4374 (M84, 3C 272.1)	E1	17.1 (2)	8.9	L2	3.5×10^{39}	5.0×10^{41}	5×10^{-6}
NGC 4486 (M87, 3C 274)	E0-1	14.9 (2)	9.8	L2	1.6×10^{40}	9.8×10^{41}	7×10^{-6}
NGC 4552 (M89)	E	14.3 (2)	8.2	T2	2.6×10^{39}	7.8×10^{40}	4×10^{-6}
NGC 4579 (M58)	SAB(rs)b	21.0 (4)	7.8	L2	1.8×10^{41}	1.0×10^{42}	1×10^{-4}
NGC 4594 (M104)	SA(s)a	9.1 (2)	8.5	L2	1.6×10^{40}	4.8×10^{41}	1×10^{-5}
NGC 4736 (M94)	(R)SA(r)ab	4.8 (2)	7.1	L2	5.9×10^{38}	1.8×10^{40}	1×10^{-5}

Notes. [a]The number in parentheses gives the source and method of the distance measurement, as follows: (1) from the catalogue of Tully & Fisher (1988), determined from a model for peculiar velocities and assuming $H_0 = 75$ km s^{-1} Mpc^{-1}; (2) from Tonry et al. (2001), who used the surface brightness fluctuation method. Following Jensen et al. (2003), the distance modulus reported by Tonry et al. (2001) was corrected by subtracting 0.16 mag; (3) from Freedman et al. (1994, 2001), who used Cepheid variables; (4) from Gavazzi et al. (1999) who used the Tully–Fisher method.
[b]L_X is the X-ray luminosity in the 2–10 keV range.
[c]The bolometric luminosities of NGC 1097, NGC 3031, NGC 3998, NGC 4374, NGC 4486, NGC 4579 and NGC 4594 were estimated by integrating the SEDs. For all other galaxies, L_{bol} was determined by scaling L_X as described in Section 2.

mass is one of the fundamental input parameters to the spectral models.

(2) Presence of a compact nuclear radio core and availability of at least one high-resolution radio detection with VLA or VLBA/VLBI. Radio measurements constrain the relative importance of the synchrotron emission from the jet and ADAF.

(3) Presence of nuclear X-ray point source and availability of its X-ray spectra. Given that the X-ray spectrum is a crucial constraint for the models, we only selected objects for which there is detected nuclear X-ray emission as opposed to upper limits.

(4) Availability of at least one high spatial resolution nuclear observation in the $1\,\mu m - 1000\,\text{Å}$ waveband. Measurements in the optical/near-IR potentially constrain the emission of the truncated thin accretion disc, whereas observations in optical/UV can constrain the inverse Compton emission produced in the inner regions of the ADAF. Therefore, we selected only sources which have at least one observation at high spatial resolution (<1 arcsec) in the $1\,\mu m - 1000\,\text{Å}$ waveband.

(5) Absence of prominent absorption features from hot stars in the nuclear UV spectrum (when available). We discarded from our analysis three sources (NGC 404, NGC 5055 and NGC 6500) from the EHF10 sample which display prominent absorption lines in their UV spectra, suggesting that stellar emission dominates the UV light (cf. Maoz et al. 1998; EHF10 for more details).

These selection criteria leave us with 12 LINERs which are listed in Table 1. This table also lists their corresponding Hubble and LINER types, black hole masses, bolometric luminosities and Eddington ratios.

We treat the observations in the IR band taken with lower spatial resolutions (>1 arcsec) – i.e. larger apertures – as upper limits because they include considerable contamination from the emission of the host galaxy.

The masses of the SMBHs were estimated from the stellar velocity dispersions using the $M_{BH}-\sigma$ relationship (Ferrarese & Merritt 2000; Gebhardt et al. 2000; Tremaine et al. 2002), with the exception of NGC 3031 (M81) and NGC 4486 (M87) whose black hole masses were estimated from the stellar and/or gas kinemat-

ics (Bower et al. 2000; Devereux et al. 2003; Gebhardt & Thomas 2009; see Table 1). As EHF10 note, for the objects with multiple mass determinations using different methods, the estimated masses are consistent with each other within a factor of 2 or better.

The OUV data of all objects were corrected for extinction (EHF10), unlike previous similar SED modelling efforts (e.g. Wu, Yuan & Cao 2007; Yuan, Yu & Ho 2009; Yu, Yuan & Ho 2011). In order to compute the bolometric luminosities from the SEDs, EHF10 used two methods. For the objects with the best sampled SEDs, they computed L_{bol} by integrating the SEDs directly, ignoring upper limit data points. These objects are NGC 3031, NGC 3998, NGC 4374, NGC 4486, NGC 4579 and NGC 4594. For these objects, they assumed that pairs of neighbouring points in the SEDs defined a power law, integrated each segment individually and summed the segments to obtain L_{bol}. From this set of best sampled SEDs, they estimated the average 'bolometric correction' from the 2–10 keV luminosity to the bolometric luminosity ($L_{bol} = 50L_X$), which they used to obtain L_{bol} for the remaining objects, for which the SEDs are not as well sampled. These bolometric luminosities are listed in Table 1.

The sources in our sample were selected based on the availability of data. As discussed by EHF10, there may be some biases inherited from the surveys from which the data were obtained which rely on objects bright in the radio, UV and X-ray bands. For instance, transition objects are under-represented while type 1.9 LINERs are over-represented. It is not clear at present whether the relative number of LINER types in our sample could impact our modelling results. Therefore, the resulting sample cannot be considered complete since it only consists of objects for which the necessary data are available. The biases resulting from this selection are difficult to quantify but we refer the reader to EHF10 for further discussion.

3 MODELS FOR THE ACCRETION FLOW AND JET

We fit the observed broad-band SEDs of the LLAGNs in our sample using a model which consists of three components: an inner ADAF, an outer truncated thin accretion disc and a jet. The components
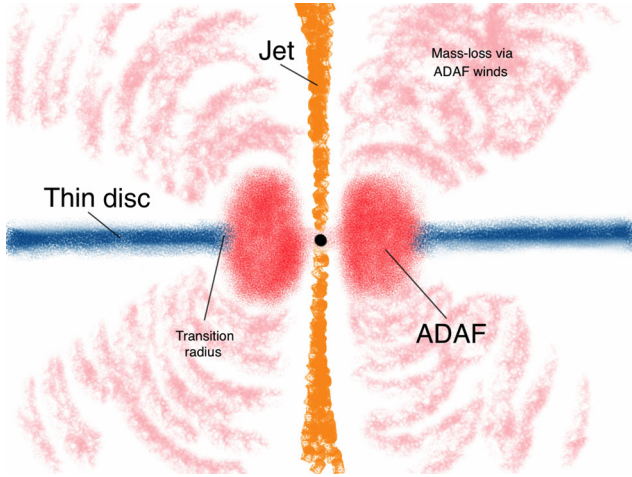
Figure 1. Cartoon illustrating the model for the central engines of LLAGNs. It consists of three components: an inner ADAF, an outer truncated thin disc and a relativistic jet.

of the model are illustrated in Fig. 1. We describe here the main features of this model.

3.1 ADAF component

The inner part of the accretion flow is in the form of an ADAF which is a hot, geometrically thick, optically thin two-temperature accretion flow, which has low radiative efficiency (e.g. Kato, Fukue & Mineshige 1998; Narayan et al. 1998). ADAFs are characterized by the presence of outflows or winds, which prevent a considerable fraction of the gas that is available at large radii from being accreted on to the black hole. This has been suggested by numerical simulations (Hawley & Krolik 2001; Stone & Pringle 2001; De Villiers, Hawley & Krolik 2003; Igumenshchev, Narayan & Abramowicz 2003; Proga & Begelman 2003; McKinney & Gammie 2004; Yuan et al. 2012) and analytical work (Narayan & Yi 1994; Blandford & Begelman 1999; Narayan, Igumenshchev & Abramowicz 2000; Begelman 2012) (cf. Narayan et al. 2012 for an alternative view). In order to take this mass-loss into account, we follow Blandford & Begelman (1999) and introduce the parameter s by

$$\dot{M} = \dot{M}_o \left(\frac{R}{R_o} \right)^s, \tag{1}$$

to describe the radial variation of the accretion rate $\dot{M}_o$ measured at the outer radius of the ADAF, R_o. The results of the numerical simulations of the dynamics of ADAFs previously mentioned as well as *Chandra* X-ray studies of NGC 3115 and Sgr A* (e.g. Wong et al. 2011; Wang et al. 2013) together with submillimetre polarization and Faraday rotation measurements of Sgr A* (Marrone et al. 2007) suggest that $0.3 \lesssim s \lesssim 1$ (the lower bound is estimated from fitting the SED of Sgr A*; cf. Yuan, Quataert & Narayan 2003; Yuan, Shen & Huang 2006). Following these results, in our models we conservatively adopt $s = 0.3$ unless otherwise noted.

The other parameters that describe the ADAF solution are the black hole mass M; the viscosity parameter α; the modified plasma β parameter, defined as the ratio between the gas and total pressures, $\beta = P_g/P_{tot}$; δ, the fraction of energy dissipated via turbulence that directly heats electrons; and the adiabatic index γ. Following Nemmen et al. (2006), in our calculations we adopt $\alpha = 0.3$, $\beta = 0.9$ and $\gamma = 1.5$. Traditional ADAF models adopted δ to be small ($\delta \lesssim 0.01$; e.g. Narayan & Yi 1995). On the other hand, it has

been argued that the value of δ can be potentially increased due to different physical processes – such as magnetic reconnection – that affect the heating of protons and electrons in hot plasmas (e.g. Quataert & Gruzinov 1999; Sharma et al. 2007). Given the theoretical uncertainty related to the value of δ, we allow it to vary over the range $0.01 \leq \delta \leq 0.5$.

The cooling mechanisms incorporated in the calculations are synchrotron emission, bremsstrahlung and inverse Comptonization of the seed photons produced by the first two radiative processes. Given the values of the parameters of the ADAF, in order to compute its spectrum we first numerically solve for the global structure and dynamics of the flow, as outlined in Yuan et al. (2000, 2003). Obtaining the global solution of the differential equations for the structure of the accretion flow is a two-point boundary value problem. This problem is solved numerically using the shooting method, by varying the eigenvalue j (the specific angular momentum of the flow at the horizon) until the sonic point condition at the sonic radius R_s is satisfied, in addition to the outer boundary conditions (Yuan et al. 2003).

There are three outer boundary conditions that the ADAF solution must satisfy, specified in terms of the three variables of the problem: the ion temperature T_i, the electron temperature T_e and the radial velocity v (or equivalently the angular velocity Ω). Following Yuan, Ma & Narayan (2008), when the outer boundary of the ADAF is at the radius $R_o = 10^4 R_S$ (where R_S is the Schwarzschild radius), we adopt the outer boundary conditions $T_{out, i} = 0.2 T_{vir}$, $T_{out, e} = 0.19 T_{vir}$ and $\lambda_{out} = 0.2$, where the virial temperature is given by $T_{vir} = 3.6 \times 10^{12} (R_S/R)$ K, $\lambda \equiv v/c_s$ is the Mach number and c_s is the adiabatic sound speed. When the outer boundary is at $R_o \sim 10^2 R_S$, we adopt the boundary conditions $T_{out, i} = 0.6 T_{vir}$, $T_{out, e} = 0.08 T_{vir}$ and $\lambda_{out} = 0.5$. After the global solution is calculated, the spectrum of the accretion flow is obtained (see e.g. Yuan et al. 2003 for more details). We verified that if these boundary conditions are varied by a factor of a few, the resulting spectrum does not change much.

3.2 Thin disc component

Our model posits that outside the ADAF there is an outer thin accretion disc with an inner radius truncated at $R_{tr} = R_o$ and extending up to $10^5 R_S$ such that the outer radius of the ADAF corresponds to the transition radius to the thin disc. The other parameters that describe the thin disc solution are the inclination angle i, the black hole mass and the accretion rate $\dot{M}_o$ (the same as the accretion rate at the outer boundary of the ADAF).

The thin disc emits locally as a blackbody, and we take into account the reprocessing of the X-ray radiation from the ADAF. This reprocessing effect has only a little impact on the spectrum of the thin disc though, with the resulting SED being almost identical to that of a standard thin disc (e.g. Frank, King & Raine 2002).

For sources without optical/UV constraints, we adopt $R_o \sim 10^4 R_S$; in this case we simply ignore the contribution of the thin disc emission since for $R_{tr} \sim 10^4 R_S$ the thin disc contributes very little to the emission compared to the ADAF. In sources for which we have available optical/UV data to constrain this component of the flow, we then explore models with $R_{tr} < 10^4 R_S$.

3.3 Jet component

The SEDs of LLAGNs are generally radio loud (Ho 1999, 2002; Ho & Peng 2001; Terashima & Wilson 2003; EHF10; but see Maoz 2007; Sikora, Stawarz & Lasota 2007). The radio prominence of these SEDs is usually explained by invoking the synchrotron emission of relativistic jets, since the accretion flow does not produce

enough radio emission to account for the observed radio luminosity (e.g. Ulvestad & Ho 2001; Wu & Cao 2005; Nemmen et al. 2006; Wu et al. 2007; Yuan et al. 2009; but see Liu & Wu 2013). Some authors even argue that the entire SED of LLAGNs may be explained by the jet component (e.g. Falcke, Körding & Markoff 2004; Markoff et al. 2008). We therefore include in our modelling the contribution from the emission from a relativistic jet.

We adopt a jet model based on the internal shock scenario which is used to interpret gamma-ray burst afterglows (e.g. Piran 1999; Spada et al. 2001; Nemmen et al. 2012; see Yuan, Cui & Narayan 2005 for more details). This model has been adopted in previous works to understand the broad-band SEDs of X-ray binaries and AGNs (Spada et al. 2001; Yuan et al. 2005; Nemmen et al. 2006; Wu et al. 2007). According to this jet model, some fraction of the material in the innermost regions of the accretion flow is transferred to the jet producing an outflow rate $\dot{M}_{\rm jet}$, and a standing shock wave in the region of the jet closest to the black hole is formed. This shock wave is created from the bending of the supersonic accretion flow near the black hole in the direction of the jet. We calculate the shock jump (Rankine–Hugoniot) conditions to find the electron and ion temperatures of the plasma ($T_{\rm e}$ and $T_{\rm i}$). We find that the jet spectrum is not very sensitive to changes in $T_{\rm e}$ and $T_{\rm i}$, since the emission is completely dominated by non-thermal electrons (see below). We therefore adopt $T_{\rm i} = 6.3 \times 10^{11}$ K and $T_{\rm e} = 10^9$ K in our calculations of the jet emission.

The jet is modelled as having a conical geometry with half-opening angle ϕ and a bulk Lorentz factor Γ_j which are independent of the distance from the black hole. The jet is along the axis of the ADAF and makes an angle i with the line of sight. The internal shocks in the jet are presumably created by the collisions of shells of plasma with different velocities. These shocks accelerate a small fraction $\xi_{\rm e}$ of the electrons into a power-law energy distribution with index p. The energy density of accelerated electrons and the amplified magnetic field are described by two free parameters, $\epsilon_{\rm e}$ and ϵ_B.

Following Nemmen et al. (2006) and Wu et al. (2007), we adopt in our calculations of the jet emission the values $\phi = 0.1$ rad, $\xi_{\rm e} = 10$ per cent and $\Gamma_j = 2.3$, which corresponds to $v/c \approx 0.9$ (except in the case of M87, which has an independent estimate of Γ_j available). For six sources we have independent constraints on the value of i (cf. Table 2). For the other six, we simply adopt $i = 30°$. Therefore, there are four free parameters in the jet model: $\dot{M}_{\rm jet}$, p, $\epsilon_{\rm e}$ and ϵ_B. We allow p to vary in the range $2-3$ as expected from shock acceleration theory. In our calculations, we consider the synchrotron emission of the jet, with the optically thick part of the synchrotron spectrum contributing mainly in the radio and the optically thin part contributing mainly in the X-rays.

3.4 Free parameters and fit procedure

Throughout this paper, we will use the dimensionless mass accretion rates $\dot{m} = \dot{M}/\dot{M}_{\rm Edd}$, noting that the Eddington accretion rate is defined as $\dot{M}_{\rm Edd} \equiv 22\,M/(10^9\,{\rm M}_\odot)\,{\rm M}_\odot\,{\rm yr}^{-1}$ assuming a 10 per cent radiative efficiency. We will also express the black hole mass in terms of the mass of the sun, $m = M/{\rm M}_\odot$, and the radius in terms of the Schwarzschild radius, $r = R/R_{\rm S}$.

We have eight free parameters in the SED fits with our coupled accretion-jet model. Four of these parameters describe the emission of the accretion flow: the accretion rate $\dot{M}_{\rm o}$, the fraction of viscously dissipated energy that directly heats the electrons δ, the transition radius between the inner ADAF and the outer truncated thin disc $R_{\rm tr}$ and the ADAF mass-loss parameter s. The other four parameters

characterize the jet emission: the mass-loss rate in the jet $\dot{M}_{\rm jet}$, the electron energy spectral index p, and the electron and magnetic energy parameters $\epsilon_{\rm e}$ and ϵ_B.

Our fitting procedure can be summarized as follows. We begin with a model characterized by the initial values $\dot{m}_{\rm o} = 0.001$, $r_{\rm tr} = 10^4$, $\delta = 0.1$, $s = 0.3$, $\dot{m}_{\rm jet} = 10^{-6}$, $p = 2.2$, $\epsilon_{\rm e} = 0.1$ and $\epsilon_B = 0.01$. We adopt an iterative procedure, in which we vary one parameter each time and keep the others fixed, computing the total emitted spectrum resulting from the sum of the radiation from the jet, truncated disc and ADAF for each iteration. We repeat this process until we obtain an acceptable fit of the total SED to the radio, optical, UV and X-ray observations. We judge the goodness of fit of the models by eye instead of using an automatic model fitting technique (e.g. maximum likelihood, Bayesian analysis, etc.). The main difficulty with implementing a more rigorous spectral model fitting is that computing the dynamics and radiative transfer for the ADAF is computationally demanding and hence the evaluation time and parameter space sampling of the models are very time consuming (see also Yu et al. 2011). Therefore, our goal is to find models which are approximately consistent with the spectral data as opposed to exhaustively exploring the full parameter space of the models.

We stress that the model components are not independent from each other. For instance, since the ADAF is connected to the thin disc at $R_{\rm o}$, the accretion rate at the ADAF outer radius is the same as the one in the truncated disc as we note in Section 7.4. Furthermore, $\dot{M}_{\rm o}$ and $\dot{M}_{\rm jet}$ are expected to be correlated and we require in our fits that $\dot{M}_{\rm jet}/\dot{M}_{\rm o} < 1$ for consistency. However, given our ignorance about the mechanism of jet formation, we vary $\dot{M}_{\rm jet}$ and $\dot{M}_{\rm o}$ independently in our fits.

Regarding the contribution of the jet to the emission, this component produces X-rays through optically thin synchrotron emission with its hardness being controlled by the parameter p; for instance, the X-ray photon index is given by $\Gamma_{\rm X} = 1 + p/2$ (e.g. Yuan et al. 2009). Since shock acceleration theory favours $2 \leq p \leq 3$ (e.g. Bednarz & Ostrowski 1998; Achterberg et al. 2001; Lemoine & Pelletier 2003), the jet model has difficulty explaining sources with $\Gamma_{\rm X} < 2$. For such sources, we favour the ADAF as the X-ray production site. On the other hand, for LLAGNs with $\Gamma_{\rm X} \geq 2$, we also consider fits to the X-ray spectrum in which the jet dominates the emission.

We have also searched the literature for independent constraints from other works on the values of the model parameters, such as the mass accretion rate, inclination angle, transition radius and jet power. We list such independent constraints in Table 2.

3.5 Contribution to the SED by stellar emission

In the optical and near-IR, even though the *HST* aperture is small (≈ 0.1 arcsec), it corresponds to $\approx 2-15$ pc for the galaxies in our sample. An ≈ 10 pc aperture will include up to a few 10^8 stars, as estimated by adopting a typical bulge stellar density of $\sim 10^5$ stars per cubic parsec (Kormendy & Kennicutt 2004). The enclosed mass is estimated roughly as

$$M_{\rm b} \sim 2 \times 10^8 \left(\frac{\rho_{\rm b}}{6 \times 10^4\,{\rm M}_\odot\,{\rm pc}^{-3}} \right) \left(\frac{R}{10\,{\rm pc}} \right)^3\,{\rm M}_\odot, \qquad (2)$$

where $\rho_{\rm b} \sim 6 \times 10^4\,{\rm M}_\odot\,{\rm pc}^{-3}$ is the typical Milky Way bulge density (e.g. Genzel, Eisenhauer & Gillessen 2010). Since typical, evolved stellar populations in bulges emit mostly in the near-IR and optical, it is prudent to consider the possible contribution of

Table 2. Model parameters resulting from the SED fits discussed in Section 4. The meaning of the parameters is described in Section 3.

Galaxy	Model	$\dot{m}_o$	r_{tr}	δ	s	$\dot{m}_{jet}$	p	ϵ_e	ϵ_B	i (°)	P_{jet}^{mod}	P_{jet}^{obs}	$\dot{m}_{Bondi}$	Refs. and notes
NGC 1097	AD	6.4×10^{-3}	225	0.1	0.8	7×10^{-7}	2.2	0.06	0.02	34	10^{43}	–	–	a, 1
NGC 3031	JD	5×10^{-4}	360	0.01	0.3	1.2×10^{-5}	2.05	0.6	10^{-4}	50	4.8×10^{42}	7.1×10^{41}	–	b
NGC 3031	AD	4×10^{-3}	360	0.035	0.3	2×10^{-6}	2.2	0.1	0.01	50	8×10^{41}	–	–	–
NGC 3998	JD	–	–	–	–	3.5×10^{-6}	2.01	0.75	3×10^{-5}	30	1.8×10^{43}	4.6×10^{42}	–	b
NGC 3998	AD	6×10^{-3}	10^4	0.05	0.3	1.7×10^{-6}	2.2	0.01	10^{-3}	30	9×10^{42}	–	–	–
NGC 4143	AD	2.5×10^{-3}	70	0.1	0.76	1.2×10^{-7}	2.2	0.03	0.1	30	1.6×10^{41}	–	–	–
NGC 4261	AD	1.9×10^{-3}	10^4	0.3	0.3	6×10^{-6}	2.2	0.01	0.1	63	2×10^{43}	–	–	–
NGC 4278	AD	7×10^{-4}	40	0.07	0.3	3.5×10^{-6}	2.3	0.001	0.01	3	4×10^{42}	–	–	3
NGC 4374	JD	–	–	–	–	1.6×10^{-6}	2.2	0.009	0.008	30	8.4×10^{42}	3.9×10^{42}	4×10^{-4}	2, 4, 5
NGC 4374	AD	2.9×10^{-3}	10^4	0.01	0.3	4×10^{-7}	2.4	0.01	0.1	30	2×10^{42}	–	–	–
NGC 4486	JD	–	–	–	–	6×10^{-8}	2.3	0.001	0.008	10	8.2×10^{42}	$10^{43} - 10^{44}$	7×10^{-4}	4, 5, 6, 7
NGC 4486	AD	5.5×10^{-4}	10^4	0.01	0.1	5×10^{-8}	2.6	0.001	0.001	10	6.8×10^{42}	–	–	–
NGC 4552	JD	–	–	–	–	1.8×10^{-6}	2.1	0.01	0.01	30	2.2×10^{42}	1.6×10^{42}	0.001	5
NGC 4579	AD	0.02	150	0.06	0.3	1.4×10^{-5}	2.2	0.011	0.008	45	5.9×10^{42}	–	–	8
NGC 4594	JD	2×10^{-3}	10^4	0.01	0.3	4.5×10^{-7}	2	0.8	0.03	30	10^{42}	3×10^{42}	0.002	b, 2
NGC 4594	AD	0.006	10^4	0.01	0.3	9×10^{-7}	2.3	0.005	0.003	30	2×10^{42}	–	–	–
NGC 4736	AD	0.0035	60	0.1	0.89	6×10^{-7}	2.2	0.01	0.01	30	6.5×10^{40}	–	–	–

Notes. (a) For NGC 1097, $\Gamma = 10$ (for consistency with the work of Nemmen et al. 2006).
(b) Observed jet power estimated using the radio data and the Merloni & Heinz (2007) correlation.
References: 1. Nemmen et al. 2006, 2. Pellegrini 2005, 3. Giroletti et al. 2005, 4. Allen et al. 2006, 5. Merloni & Heinz 2007, 6. Biretta et al. 1999, 7. Di Matteo et al. 2003, 8. Barth et al. 2001.

unresolved, nuclear stellar population at these wavebands in our sample. Thus, for the 12 LLAGNs for which we have optical observations available, we also consider the possibility that the nuclear optical data are reproduced with simple stellar population spectral models.

We adopt a 10-Gyr-old stellar population with solar metallicity and a Salpeter initial mass function as representative of the typical evolved stellar populations in galactic bulges (Wyse, Gilmore & Franx 1997). We perform a least-squares fit of the compact nuclear stellar population spectral model (Bruzual & Charlot 2003) to the *HST* optical measurements (and to the optical spectrum in the case of NGC 1097) by simply varying the mass of the stellar population. The resulting stellar population spectral models are displayed alongside the accretion flow and jet models in Figs 2–8, for illustration. We did not try to perform a detailed simultaneous fit of the accretion flow/jet models and the stellar population to the observations. We simply want to illustrate the potential of unresolved stellar populations to account for the optical observations.

Given that the luminosity of the stellar population falls quite rapidly for $\lambda < 4000$ Å and that LINERs tend to be UV variable with the UV flux setting a lower limit to the AGN luminosity (Maoz et al. 2005; Maoz 2007), we only consider the high-resolution *HST* observations with $\lambda < 4000$ Å in the stellar population spectral fits.

We note that the IR upper limits in the SEDs are consistent with the contribution of an old stellar population to the near-IR spectral region due to the large apertures of these observations. This is illustrated in Fig. 2 but is also the case for the other galaxies with similar upper limits in our sample.

4 SED FITTING RESULTS

We describe in this section the results obtained from fitting our coupled accretion-jet model to the SEDs. In the SED plots that
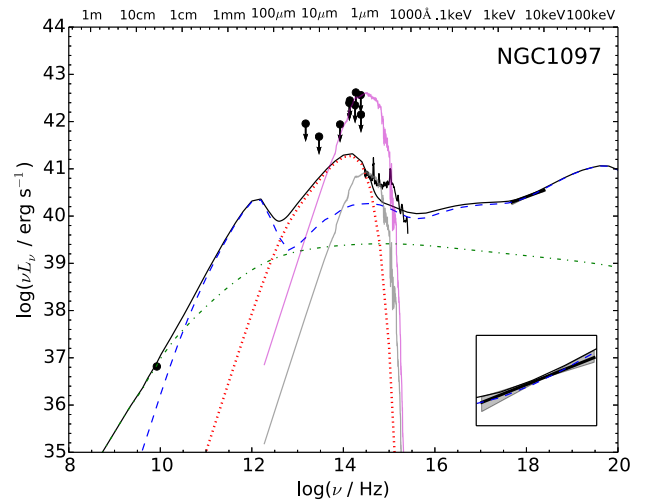
Figure 2. The observed SED and ADAF-dominated model for NGC 1097. The dashed blue, dotted red and dot–dashed green lines correspond to the emission from the ADAF, truncated thin disc and jet, respectively. The solid black line represents the sum of the emission from all components. The inset shows the zoomed 2–10 keV spectrum. The upper solid magenta line shows the spectrum of an old stellar population with $\sim 7 \times 10^9$ M$_\odot$ which accounts for the near-IR upper limits observed at lower spatial resolution. The lower solid grey line displays the spectrum of an old stellar population fitted to the optical observations.

follow below, the points in the OUV waveband correspond to the data without any extinction correction while the upper bars represent the same observations after a maximal extinction correction (see EHF10); hence, these bars illustrate the uncertainty in the extinction corrections.
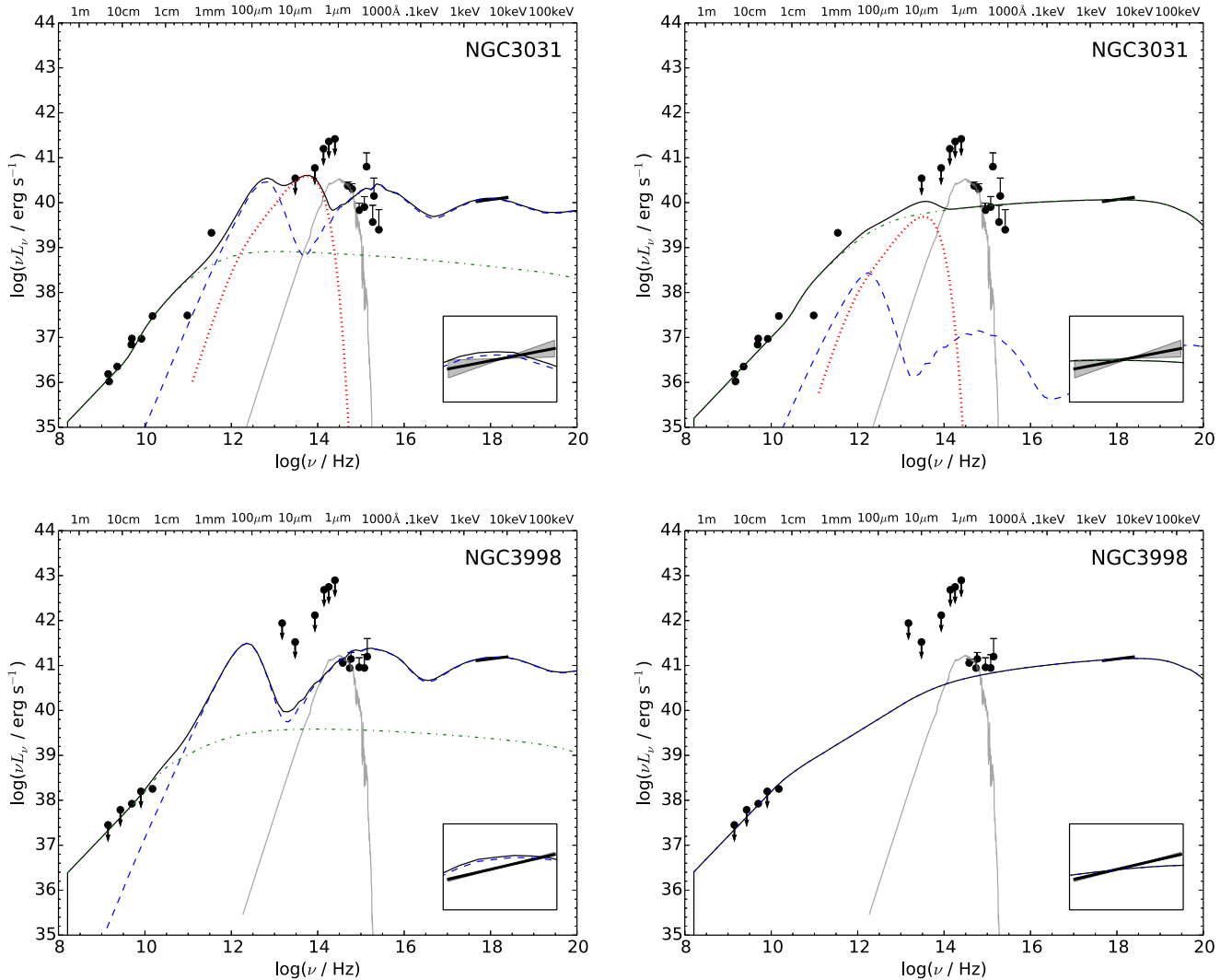
Figure 3. SEDs and coupled accretion-jet models for NGC 3031 and NGC 3998. The left-hand panel shows the AD models for each object while the right-hand panel displays the JD models. The dashed, dotted and dot–dashed lines correspond to the emission from the ADAF, truncated thin disc and jet, respectively. The solid line when present represents the sum of the emission from all components. The inset shows the zoomed 2–10 keV spectrum. The old stellar population fitted to the optical data is displayed as the grey solid line.

The arrows represent upper limits to the nuclear luminosity. These upper limits are either a result of non-detections or because the corresponding observations were taken through a large aperture (>1 arcsec). In the latter case, the upper limits include a potentially significant contribution by the emission from dust and the stellar population of the galaxy bulge as discussed in the previous section. In order to illustrate this point, we consider the case of NGC 1097. The IR observations for this LINER were taken through an aperture of diameter ≈5 arcsec (Nemmen et al. 2006) which corresponds to ≈364 pc. The bulge stellar mass enclosed within this aperture can be roughly estimated using equation (2) as ∼7 × 10⁹ M⊙. Fig. 2 shows the spectrum of an old stellar population with this amount of mass, demonstrating that the bulge stellar emission can account for at least part of the IR upper limits in our sample. Therefore, even though the IR upper limits are not very useful to constrain the

accretion and jet models, we display the corresponding data points in Figs 3–9 for completeness.

Table 2 lists the model parameters. We list whenever available the Bondi accretion rate and the corresponding reference from which $\dot{m}_{\rm Bondi}$ was taken. $P_{\rm jet}^{\rm obs}$ corresponds to the jet power estimated either from observations or using the correlation between the jet power and radio luminosity of Merloni & Heinz (2007). $P_{\rm jet}^{\rm mod}$ represents the jet power resulting from our jet model, calculated as $P_{\rm jet} = \dot{M}_{\rm jet}\Gamma_j^2 c^2$. Table 3 shows the stellar mass potentially enclosed within 0.1 arcsec as obtained from the stellar populations fits to the *HST* optical observations.

For completeness, we present model fits to the nine SEDs from EHF10 which did not pass our data quality cut in Appendix B. However, due to the lower quality of their SEDs, we refrain from drawing conclusions based on those sources.
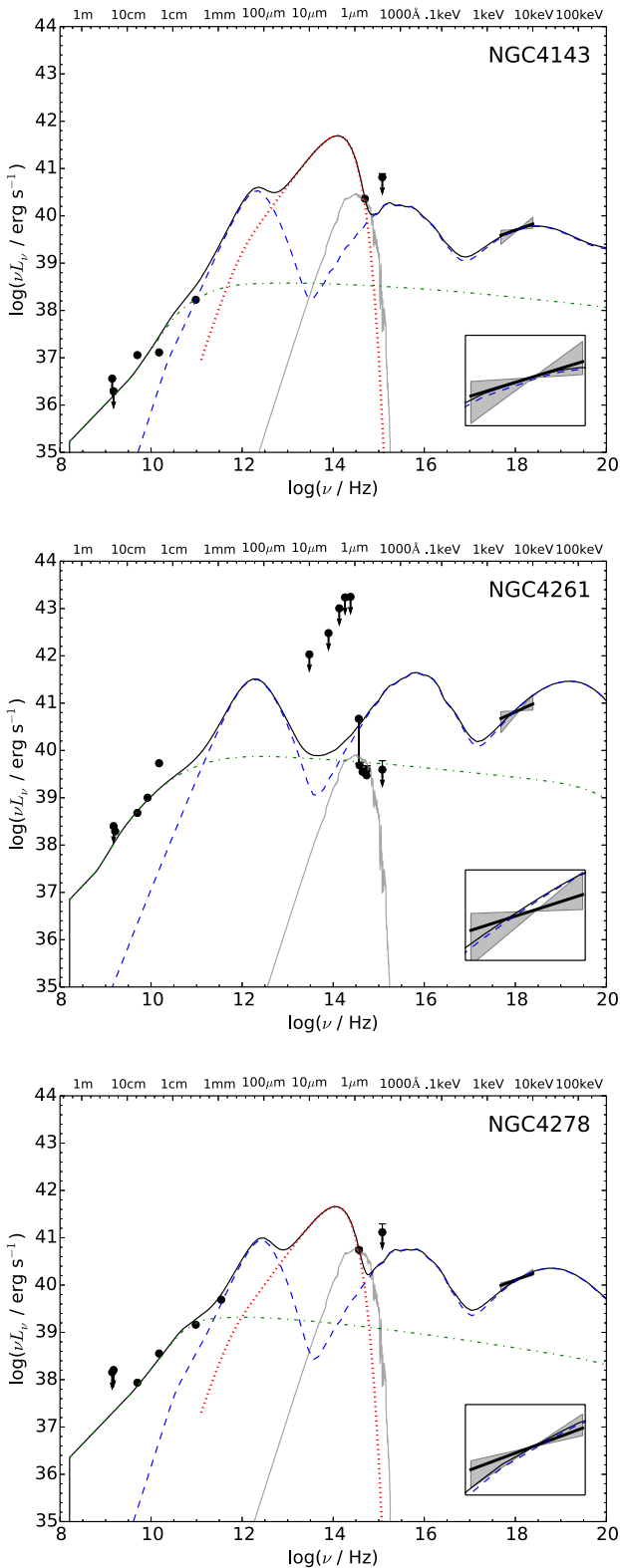
Figure 4. Same as in Fig. 3 for NGC 4143, NGC 4261 and NGC 4278, displaying only AD models.

We demonstrate in this section that there are two possible types of models which can accommodate the observed SED of M81 (and the SEDs of other LINERs in our sample as we will show below). In the first type, the emission from the ADAF dominates the

observed X-rays; in the second type of model, the jet emission dominates the X-rays. We will hereafter use the abbreviations AD (as in *ADAF-dominated*) and JD (as in *jet-dominated*) when referring to the former and latter types of models, respectively.

4.1 NGC 1097

The SED of this object was previously studied in detail by Nemmen et al. (2006) and the model displayed in Fig. 2 corresponds to the model obtained by Nemmen et al. (2006). The transition radius is independently constrained from the modelling of the broad double-peaked Hα emission line ($r_{tr} \sim 225$). Once the transition radius is fixed and requiring that the accretion rate in the outer thin disc is the same as in the outer parts of the ADAF, there is not much flexibility in the resulting thin disc spectrum; as such, the truncated thin disc spectrum self-consistently reproduces the *HST* optical data (Nemmen et al. 2006). The jet emission accounts for the radio data point while the hard X-ray spectrum from the ADAF accounts for the *Chandra* observations. The jet emission is not able to reproduce the X-ray spectrum since it would require $p < 2$ (see Section 3.4). Our models do not take into account the contribution of the nuclear starburst in the UV. Therefore, they do not reproduce the 'UV bump' between ≈ 1000 and ≈ 7000 Å (see fig. 3 in Storchi-Bergmann et al. 2005).

Fig. 2 also illustrates that we cannot rule out the possibility that the optical emission is produced by an unresolved, old stellar population located within 0.1 arcsec with a mass $1.5 \times 10^{8} \, M_{\odot}$ (cf. Section 3.5).

The IR upper limits, observed with a lower spatial resolution, are consistent with an old stellar population with a mass $\sim 7 \times 10^{9} \, M_{\odot}$. As discussed in the previous section, this is presumably the case for the other galaxies in our sample which also have lower spatial resolution IR observations, although the stellar mass will vary from source to source.

4.2 NGC 3031

This source is among the brightest LLAGNs known since it is the nearest AGN besides Centaurus A and has been the subject of a broad-band multiwavelength monitoring campaign (Markoff et al. 2008; Miller et al. 2010).

Devereux & Shearer (2007) modelled the profile of the broad double-peaked Hα line with a relativistic thin disc model. They were able to explain the profile with an inclination angle of 50°. Such a high inclination angle is supported by radio observations of the jet (Bietenholz, Bartel & Rupen 2000). The Hα line profile of M81 is consistent with an inner radius of $\approx 280 - 360 R_S$ for the line-emitting thin disc (Devereux & Shearer 2007). In our models for the SED, we therefore adopt $i = 50°$ and $r_{tr} = 360$. The resulting IR-luminous thin disc spectrum is not strongly constrained by the available IR upper limits and OUV observations. On the other hand, the optical data points at 6000 and 4700 Å are consistent with a stellar population with mass $6.2 \times 10^{7} \, M_{\odot}$.

Fig. 3 shows two models for the SED of M81 consistent with the above constraints: on the left-hand side, an ADAF with $\delta = 0.01$ dominates the X-ray emission whereas in the model to the right a jet with $p = 2$ is the dominant X-ray emitter.

4.3 NGC 3998

The shortest wavelength (1750 Å) UV data point in the SED of NGC 3998 presented in EHF10 is anomalously high because of
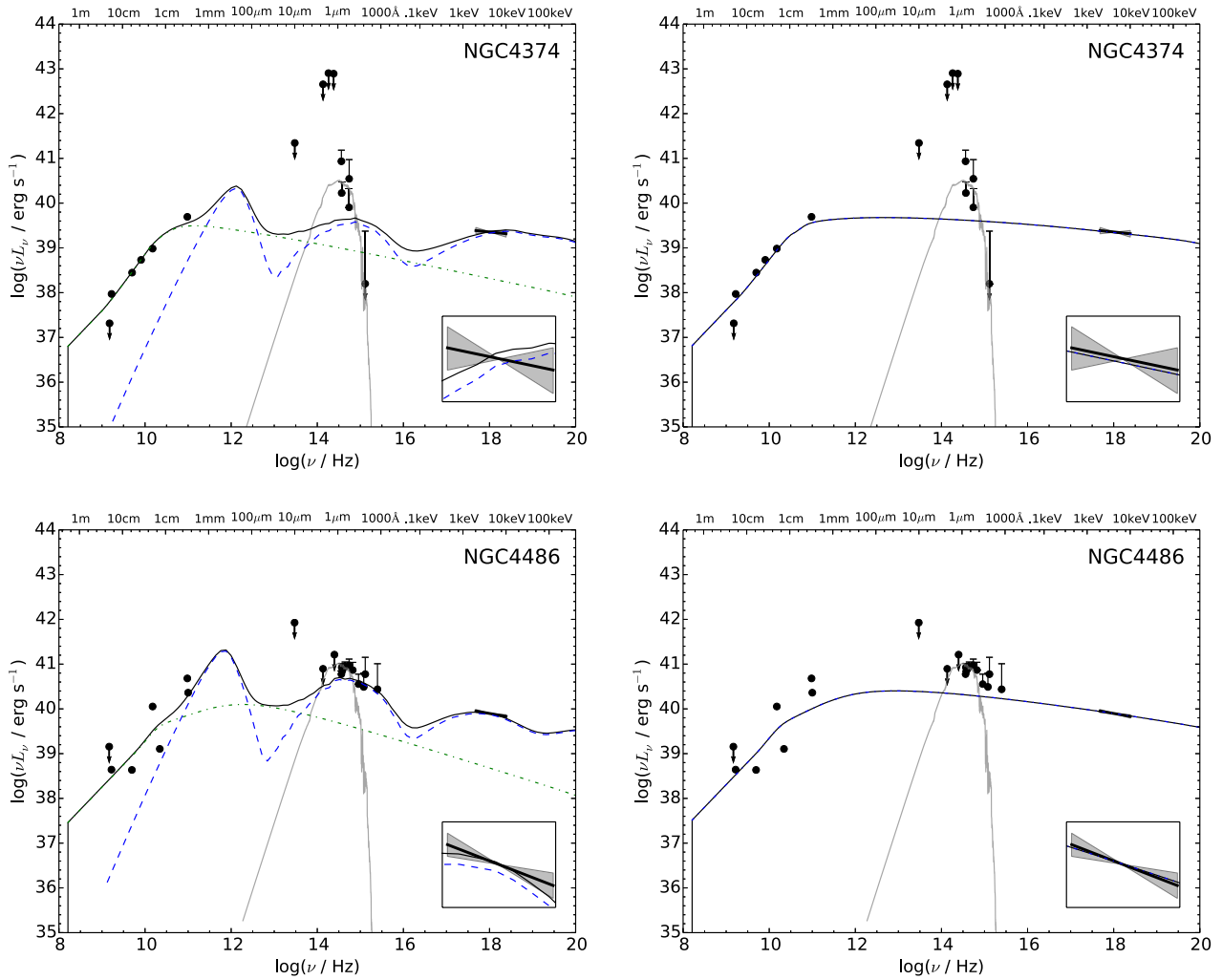
Figure 5. Same as Fig. 3 for NGC 4374 and NGC 4486.

variability (Devereux 2011). As discussed by Devereux, this data point was obtained many years before all the other observations, when the source was much brighter. For this reason, we exclude this UV measurement from our analysis and plots.

In our models we adopted a large outer radius for the ADAF, but smaller radii are not ruled out by the data. For instance, we are also able to obtain a reasonable fit to the SED with $r_{tr} = 500$ and $\dot{m}_o = 10^{-3}$. This model is consistent with the IR upper limits and accounts for the X-ray data. The transition radius cannot be much smaller than this value, otherwise the emission of the truncated thin disc would exceed the IR upper limits. Furthermore, as noted by Ptak et al. (2004), the lack of Fe Kα line emission also suggests that the value of r_{tr} is not so small.

A JD model accounts quite well for the X-rays but somewhat underestimates the OUV data.

4.4 NGC 4143

The optical data point can be reproduced by emission from the truncated thin disc emission with the somewhat small transition radius of $r_{tr} = 70$. Alternatively, the optical observation can be fitted with an old stellar population with mass $5 \times 10^7 \, M_{\odot}$. Since

the jet model requires $p < 2$ to reproduce the X-ray spectrum, a jet origin for the X-ray emission in disfavoured.

4.5 NGC 4261

Estimates of the Bondi rate, inclination angle and jet power are available (Gliozzi, Sambruna & Brandt 2003; Merloni & Heinz 2007), and there are two independent estimates of the jet power. We adopt $i = 63°$ in our models (Gliozzi et al. 2003). The accretion rate we obtain from the ADAF fit is somewhat smaller than $\dot{m}_{Bondi}$. A jet origin for the X-rays is disfavoured since it would require $p < 2$.

This AGN is likely to be strongly affected by extinction in the OUV band (EHF10). Hence, the OUV measurements probably do not capture the emission of the central engine. For this reason, it is not surprising that the models overpredict the OUV emission by almost one order of magnitude in Fig. 4.

4.6 NGC 4278

Di Matteo, Carilli & Fabian (2001) also estimated that the Bondi rate is $\dot{m}_{Bondi} \sim 0.001 - 0.01$. Giroletti, Taylor & Giovannini (2005) found a two-sided radio structure for the jet using VLA data, and

estimated that the jet is oriented close to the line of sight ($2° \lesssim i \lesssim$ $4°$) and mildly relativistic ($\Gamma_j \sim 1.5$). In our jet models, we therefore adopt $i = 3°$ and $\Gamma_j = 1.5$.

The optical data point requires a truncated thin disc with the somewhat small transition radii $r_{tr} \sim 30-40$. If we allow s to vary, we can also reproduce the SED with a larger transition radius, $r_{tr} = 100$, $\dot{m}_o = 4 \times 10^{-3}$, $\delta = 0.1$ and $s = 0.77$. Alternatively, the optical observation can be fitted with a $10^8\,M_\odot$ stellar population. A JD model is disfavoured for this source.

4.7 NGC 4374

A prominent jet resolved with the VLA is observed to create cavities in the X-ray emitting gas (Allen et al. 2006; Finoguenov et al. 2008).

We find adequate AD and JD models for the data. As was the case for NGC 4594, the mid- to near-IR data are insufficient to make the case of a truncated thin disc compelling, and similar models with much larger values of r_{tr} are not ruled out by the available IR data. The jet power in both models is in good agreement with the power estimated by Merloni & Heinz (2007) based on the calorimetry of the X-ray cavities observed with *Chandra*. A $5 \times 10^7\,M_\odot$ stellar population nicely reproduces the optical excess above the models.

4.8 NGC 4486

Di Matteo et al. (2003) previously estimated the Bondi accretion rate using *Chandra* X-ray data ($\dot{M}_{Bondi} \sim 0.1\,M_\odot\,yr^{-1}$; $\dot{m}_{Bondi} \approx 7 \times 10^{-4}$). Biretta, Sparks & Macchetto (1999) analysed *HST* observations of the jet in M87 and estimated that $\Gamma_j \geq 6$ and $10° < i < 19°$. Based on the results of Biretta et al. (1999), we adopt in our jet modelling the parameters $\Gamma_j = 6$ and $i = 10°$. The jet kinetic power is estimated to be in the range $10^{43}-10^{44}$ erg s^{-1} (e.g. Bicknell & Begelman 1999; Owen, Eilek & Kassim 2000; Allen et al. 2006; Merloni & Heinz 2007).

We find adequate AD and JD models for the data, although the JD model underpredicts the OUV data by a factor of a few. The SED of M87 was previously fitted using ADAF and/or jet models (Di Matteo et al. 2003; Li et al. 2009; Yuan et al. 2009). Di Matteo et al. (2003) modelled the SED of M87 with an ADAF model using different values of δ but not including mass-loss (i.e. $s = 0$). The model adopted by Li et al. (2009) is quite similar to that of Di Matteo et al. (2003) although the former incorporate general relativistic corrections. Di Matteo et al. (2003) and Li et al. (2009) obtained that the ADAF emission with no mass-loss approximately reproduces the SED and results in accretion rates consistent with the Bondi rate. Our AD model is similar to that of Di Matteo et al. (2003) but it also incorporates mass-loss as suggested by numerical simulations.

Yuan et al. (2009) tried to model the SED using an ADAF model with $\delta = 0.5$ but failed to fit to data with an AD model. The reason is that for high values of δ ($\delta > 0.1$) and small accretion rates ($\dot{m}_o \ll 0.01$), the ADAF X-ray spectrum is harder than the data. Yuan et al. (2009) instead successfully fit the data with a JD model using $p = 2.5$ similarly to our JD model.

4.9 NGC 4552

The Bondi accretion rate was estimated by Merloni & Heinz (2007) (see also Allen et al. 2006) from the X-ray profiles of density and temperature. The kinetic power carried by the jet was estimated by Merloni & Heinz (2007) (see also Allen et al. 2006) from the energy deposited in the X-ray cavities. Since the X-ray spectrum is quite
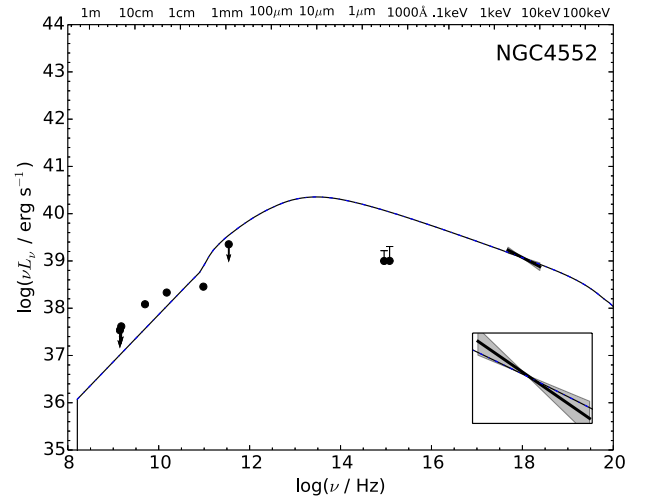

Figure 6. The SED and jet-dominated model for NGC 4552. The inset shows the zoomed 2–10 keV spectrum.
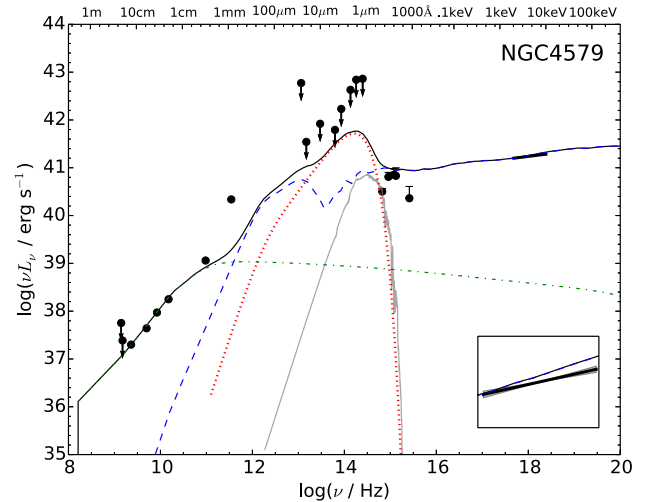

Figure 7. Same as Fig. 2 for NGC 4579 (AD model).

soft, AD models are unable to account for the X-ray emission. The JD model in Fig. 6 is roughly consistent with the radio observations and explains quite well the X-ray data, but overpredicts the optical data. The resulting jet power is roughly consistent with the value estimated by Allen et al. (2006) and Merloni & Heinz (2007). A likely explanation for the unusually faint UV emission compared to the X-rays is source variability (Maoz et al. 2005) and hence we did not attempt to fit the 2500 and 3300 Å measurements with a stellar population as in the other LLAGNs.

4.10 NGC 4579

NGC 4579 shares many characteristics with NGC 3031 (M81) and NGC 1097: its nucleus features broad double-peaked Balmer emission lines (Barth et al. 2001) and a lack of the iron Kα line emission (Eracleous et al. 2002). From the width of the broad Hα line, Barth et al. (2001) obtained a rough estimate of the inner radius of the line-emitting portion of the accretion disc $r_{tr} \sim 160$. Hence, we adopt in our SED models $r_{tr} = 150$ and $i = 45°$. The resulting thin
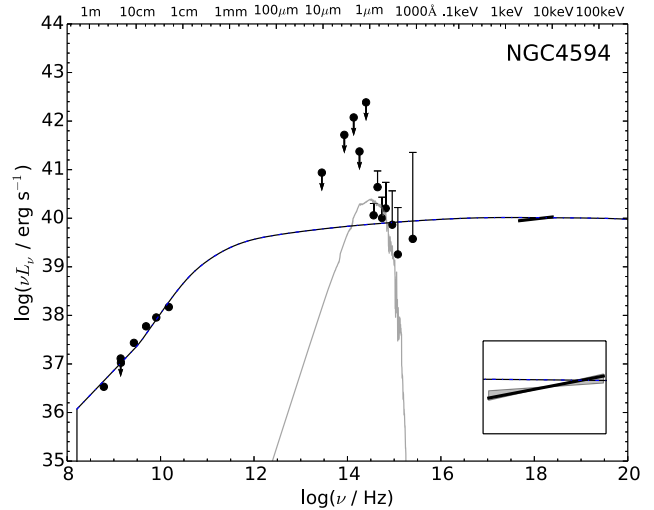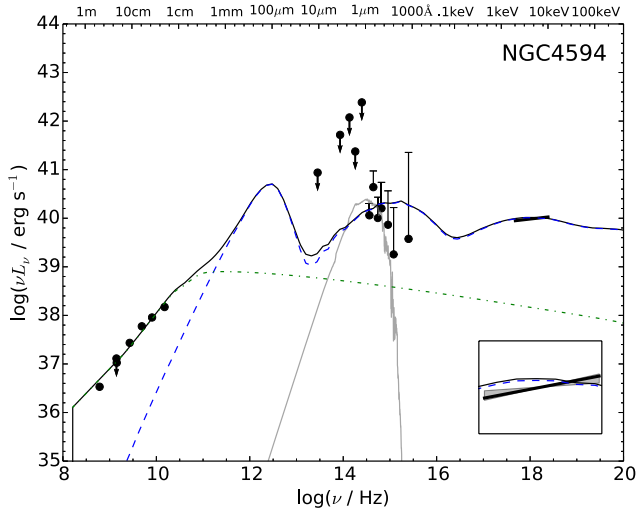
Figure 8. Same as Fig. 3 for NGC 4594.

disc spectrum peaks in the IR and its high-frequency tail extends into the OUV; however, the available IR upper limits and *HST* OUV data do not allow us to set strong constraints on the thin disc emission. A jet origin for the X-rays is disfavoured by the hardness of the spectrum.

4.11 NGC 4594

The left-hand panel of Fig. 8 shows an AD model which is consistent with the available OUV and X-ray data. In this model, the jet dominates the radio emission and contributes only weakly to the X-ray flux. The inferred accretion rate is consistent with the Bondi accretion rate estimated by Pellegrini (2005). The available data are not sufficient to constrain the presence of a truncated thin disc in this source; hence, we adopt $r_{tr} = 10^4$. The right-hand panel of Fig. 8 shows a jet model for the SED of NGC 4594 which is consistent with the data for $p = 2$.

4.12 NGC 4736

As was the case of NGC 1097, NGC 4143 and NGC 4278, this LINER requires a relatively small transition radius in order to explain its UV data. The 3300 Å observation can also be reproduced by an $\approx 1.2 \times 10^8 \, M_\odot$ stellar population. The X-ray spectrum is too hard to be explained by a jet model (Fig. 9).

5 CONSTRAINTS ON THE ACCRETION-JET PARAMETERS

Our detailed SED modelling allows us to place constraints – within the framework of ADAF and jet models – on the mass accretion rate on to the black hole and kinetic power for the LLAGNs in our sample. In this section, we evaluate possible correlations among the parameters describing the accretion flow and jet resulting from our SED models. In particular, when discussing correlations between the mass accretion rate and other parameters, we restrict ourselves only to AD models. The reason is that in most JD fits the estimate of $\dot{m}$ that we obtain from the fits should be regarded as a rough lower limit to the accretion rate. In fact, for most of the JD models, the contribution of an underlying ADAF to the emission is not
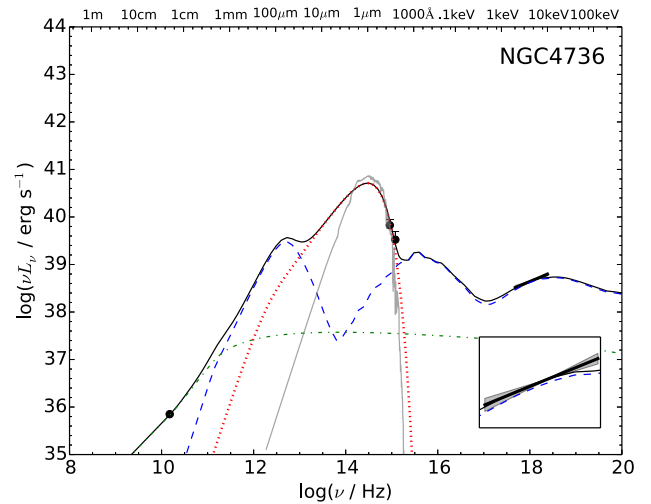

Figure 9. Same as Fig. 2 for NGC 4736 (AD model).

necessarily required (cf. the JD models for NGC 4594, M87 and NGC 4579).

We show in panel (a) of Fig. 10 the relation between the accretion rate at the outer radius of the ADAF and the global radiative efficiency of the systems, defined as $\eta_{rad} \equiv L_{bol}/(\dot{M}_o c^2)$ where we obtain L_{bol} by integrating the synthetic spectra obtained in the SED fits including all components (thin disc, ADAF and jet). The values of η_{rad} for our sample are in the range $\sim(10^{-3}-1)$ per cent while the accretion rates are in the range $\dot{m} \approx 10^{-4}-0.01$. There is no apparent correlation between the global efficiency and $\dot{m}_o$, keeping in mind the significant uncertainties in $\dot{m}_o$ and L_{bol}. The error bars are estimated as described in Appendix A.

Panel (b) of Fig. 10 shows the relation between the accretion rate and the jet power in Eddington units, while panel (c) displays the relation between the accretion rate and jet kinetic efficiency $P_{jet}/(\dot{M}_{BH} c^2)$ defined in terms of the accretion rate at $3R_S$, $\dot{M}_{BH} \equiv \dot{M}(3R_S)$. Panel (b) shows that there is a hint of a correlation which is significant at the $\approx 2\sigma$ level. However, panel (c) shows no clear evidence for a correlation between the accretion rate and the kinetic efficiency.
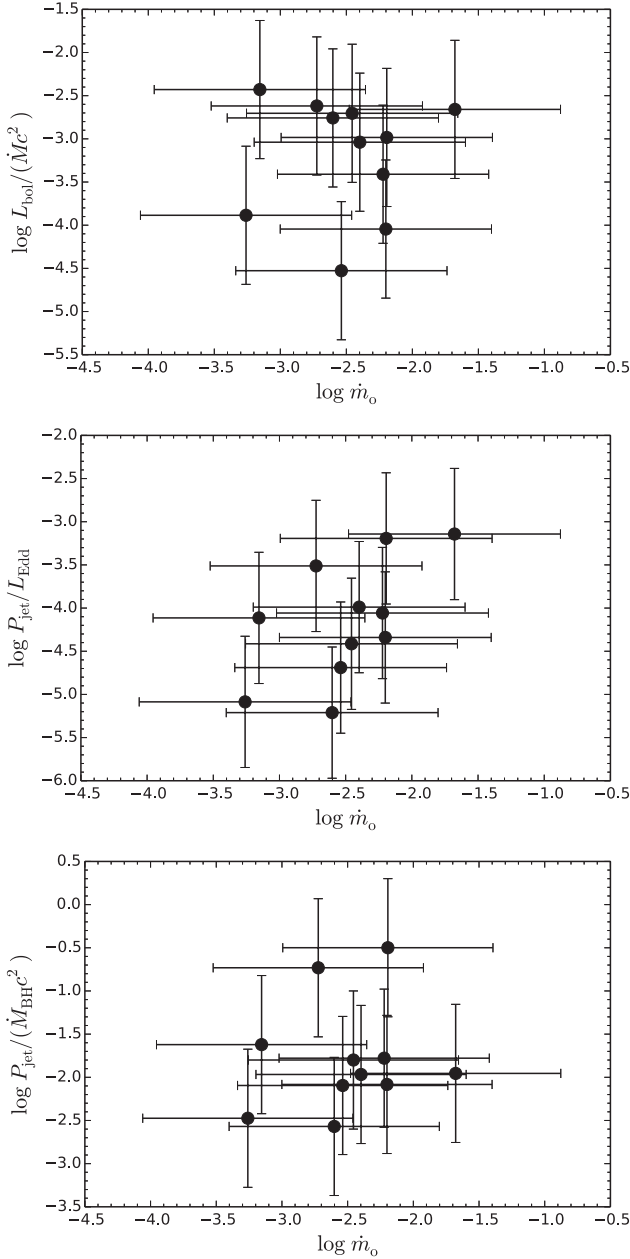
Figure 10. The relation between the mass accretion rate $\dot{m}_o$ at the outer radius of the ADAF (in Eddington units) and the global radiative efficiency [$L_{bol}/(\dot{M}_o c^2)$] (panel a, top), jet power normalized in Eddington units (panel b, centre) and the jet kinetic efficiency defined in terms of the accretion rate at $3R_S$ (panel c, bottom). The error bars are estimated as described in Appendix A.

Low-power radio galaxies exhibit a correlation between the jet power – derived from X-ray cavities which were presumably created by the AGN outflows – and the Bondi accretion rates $\dot{M}_{Bondi}$ – inferred from the density and temperature profiles that are obtained from the X-ray observations (Allen et al. 2006; Balmaverde, Baldi & Capetti 2008; but see Russell et al. 2013). The Bondi rates are usually parametrized in the literature as a 'Bondi power' assuming a 10 per cent efficiency ($P_{Bondi} \equiv 0.1\dot{M}_{Bondi}c^2$). Therefore, in order to compare our results with these independent estimates of jet powers
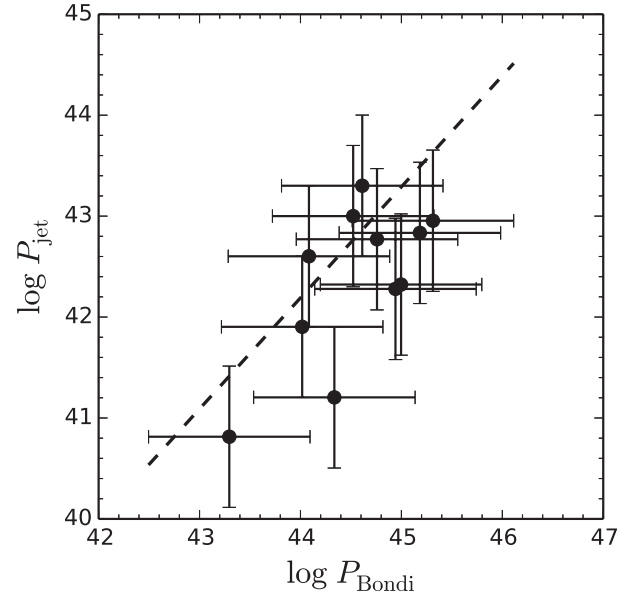
Figure 11. The relation between the Bondi power P_{Bondi} as defined in equation (3) and the jet power, using the parameters inferred from the SED models in our sample. The dashed line corresponds to the $P_{Bondi}-P_{jet}$ relation obtained by Balmaverde et al. (2008).

and $\dot{M}_{Bondi}$, we use the accretion rates that we derived to define the 'Bondi power'

$$P_{Bondi} \equiv 0.1\dot{M}_o c^2/\alpha, \qquad (3)$$

taking into account that $\dot{M}_o = \alpha\dot{M}_{Bondi}$ in the ADAF model (Narayan & McClintock 2008). Fig. 11 displays the relation between P_{Bondi} defined using the equation above and the jet powers we derived from our SED models. The uncertainties in P_{Bondi} and P_{jet} are both ~0.8 dex (see Appendix A). For illustration, we also show in Fig. 11 the relation between P_{Bondi} and P_{jet} derived by Balmaverde et al. (2008). Within the uncertainties, we can see that our SED fitting results are consistent with the Balmaverde et al. correlation.

We then proceed to estimate the radio loudness parameter from the SED fits. The radio loudness can be quantified as the optical-to-radio ratio $R_o \equiv L_\nu(6\,cm)/L_\nu(B)$ (Kellermann et al. 1989) where radio-quiet objects correspond to $R_o = 10$. Fig. 12 shows the relation between R_o and the mass accretion rate. There is a hint of an anticorrelation between these variables, significant at the 1.6σ level (keeping in mind the non-negligible uncertainties). This is in general agreement with previous evidence for an anticorrelation between radio loudness and the Eddington ratio in radio-loud AGNs (Ho 2002; Sikora et al. 2007; Broderick & Fender 2011).

We consider the relation between the X-ray luminosity and the bolometric luminosity. Fig. 13 displays the correlation between L_X and L_{bol} as well as the corresponding uncertainties. These variables display a correlation significant at the 3.4σ level. We perform a linear regression using the least-squares bivariate correlated errors and intrinsic scatter ($Y|X$) method with bootstrapping (Akritas & Bershady 1996). The best-fitting model corresponds to the solid line ($\log L_{bol} = A \log L_X + B$; shaded region corresponds to the 1σ confidence band). The best-fitting parameters are $A = 0.63 \pm 0.12$ and $B = 16.3 \pm 4.9$. The scatter about the best fit is 0.3 dex.
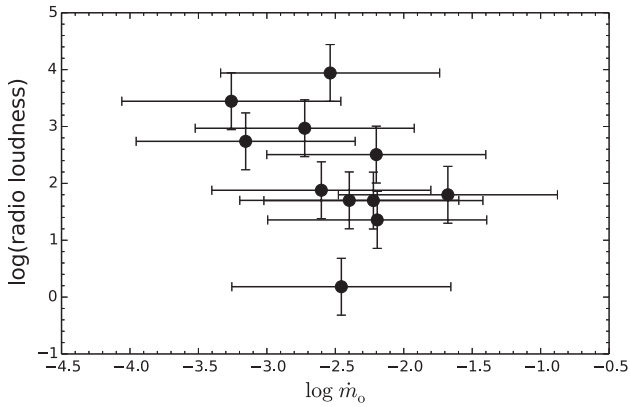
Figure 12. Relation between the mass accretion rate $\dot{m}_o$ and the radio loudness R_o. The anticorrelation is only significant at the 1.6σ level.
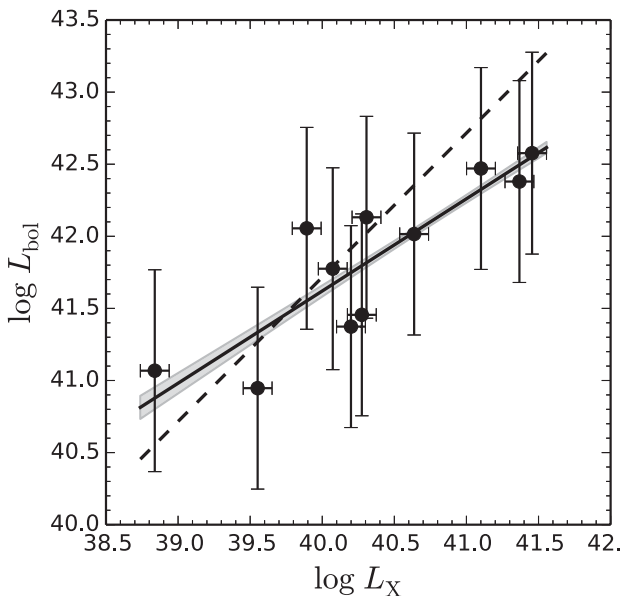
Figure 13. The relation between $2-10$ keV X-ray luminosity and the bolometric luminosity. The solid line shows the best-fitting power-law model as described in the text (shaded region, 1σ confidence band). The dashed line corresponds to $L_{bol} = 52L_X$ as in EHF10.

Hence, this result suggests that the best-fitting $2-10$ keV X-ray bolometric correction is given by

$$\kappa_X \approx 13 \left(\frac{L_X}{10^{41} \text{ erg s}^{-1}} \right)^{-0.37}. \qquad (4)$$

EHF10 performed a linear interpolation (in log space) of the SED data points of a control sample of seven LLAGNs and estimated the median X-ray bolometric correction as 52. Within the uncertainties, this bolometric correction is consistent with our results, as can be seen in Fig. 13 (dashed line corresponds to $L_{bol} = 52L_X$). We discuss how our values of κ_X compare to those typical of quasars in Section 7.3.

Finally, we computed the α_{ox} parameter for our sample of AD model SEDs. α_{ox} is a simple parametrization of the UV-to-X-ray ratio defined in terms of the spectral index of a power law between L_ν at 2500 Å and at 2 keV defined as $\alpha_{ox} \equiv 0.384 \log [L_\nu(2 \text{ keV})/L_\nu(2500 \text{ Å})]$. We find a median value for α_{ox}

of -1.1 with a standard deviation of 0.1. An extrapolation of the $\alpha_{ox}-L_\nu(2500 \text{ Å})$ relation obtained from Seyferts and quasars (Steffen et al. 2006; Young, Elvis & Risaliti 2009) to the low luminosities typical of our sample predicts α_{ox} values in the range $-0.9 \lesssim \alpha_{ox} \lesssim -0.6$. Therefore, the typical α_{ox} values in our sample of LLAGNs seem to be lower than what would be expected based on a direct extrapolation of trends obtained from brighter AGNs. We caution the reader, however, that our α_{ox} estimates should be regarded with caution. For instance, given the uncertainty in the degree of extinction affecting the UV luminosities in our sample, we estimate that uncertainties as high as ~ 0.5 dex in $L(2500 \text{ Å})$ – and correspondingly in α_{ox} – are likely (cf. Appendix A).
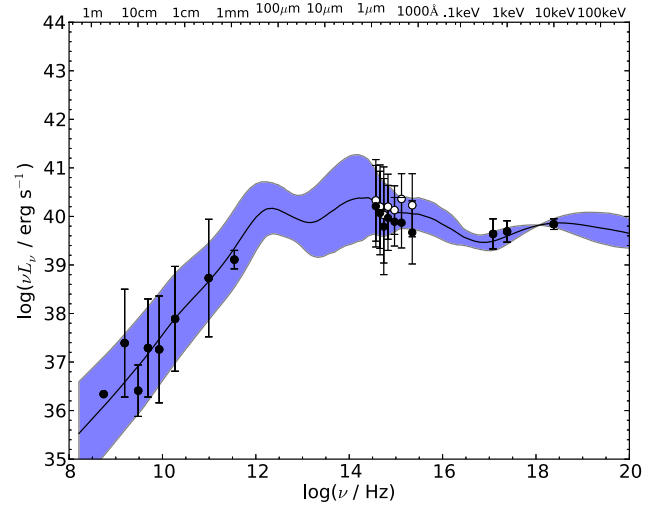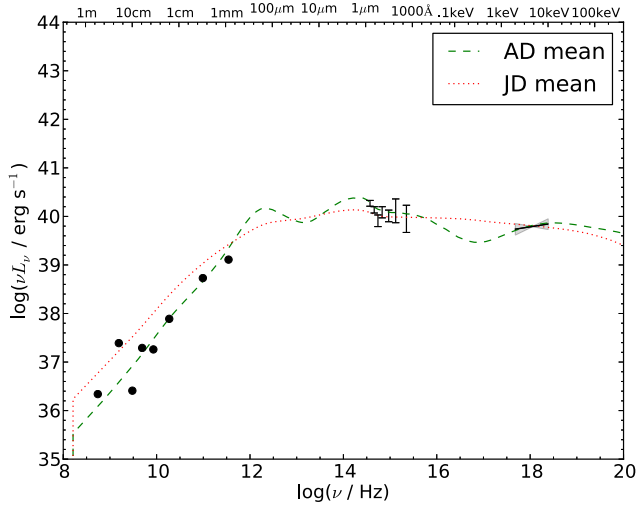
6 THE AVERAGE SED

It is of interest to compute the average SEDs resulting separately from the AD and JD scenarios. These SEDs are useful for different purposes. Since the observed SEDs are the main observables that we use to derive the central engine parameters via our fitting, as a consistency check the average model SEDs should reproduce the average SED obtained directly from the observed ones.

Secondly, SEDs obtained from averaging observed data points are obviously limited by the observed bands. Outside the observed bands different authors adopt ad hoc interpolations between the data, usually a linear interpolation in log–log space (Ho 1999; EHF10), which might not reflect the actual physical processes involved in the emission. The average from the AD and JD scenarios that we obtained can hence serve as guidelines – with a physical justification – to the typical shape of the SEDs in the bands which have not been constrained yet.

Motivated by the reasons above, we show in Fig. 14(a) the average SEDs computed separately for the AD and JD scenarios. We first normalized the individual SEDs to the same X-ray luminosity of 10^{40} erg s^{-1} in the band 2–10 keV. This value is approximately the average X-ray luminosity for the LINERs in our sample. After normalizing the SEDs, for each frequency bin we computed the mean of the model SEDs as $\langle \log \nu L_\nu \rangle$. Following EHF10, we choose to compute the average of the logarithm of the luminosities instead of using the values of νL_ν themselves in order to reduce the effect of outliers in the resulting average.

The average JD SED is relatively featureless and has a small bump in the IR between a few $\times 10$ μm and a few $\times 1$ μm which is due to the truncated thin disc. The average AD SED on the other hand is more complex given the richer variety of radiative processes which take place. Overall, the spectral shapes of the average JD and AD SEDs are similar. The bumps in the average SEDs are much less pronounced than the bumps in the individual SEDs. This occurs because the bumps in the individual SEDs do not peak at the same place and when the SEDs are averaged these bumps are smoothed out. For this reason, the average model SEDs will not resemble any one of the individual SEDs.

Fig. 14(a) also displays the average data points computed from the observed SEDs in a similar way by EHF10 where the error bars represent the uncertainty in the emission due to the uncertainty affecting the amount of extinction correction involved. The shaded region around the average best-fitting X-ray power law represents the standard deviation in the value of the LINER photon index. In order to illustrate the wide diversity of the individual SEDs, we show in Fig. 14(b) the 1σ scatter affecting the model SEDs (where we show only the AD average SED for simplicity) and the observed ones.

Figure 14. Panel a (left): the average SEDs (geometric mean) computed separately for the AD and JD models (dashed and dotted lines, respectively). The data points correspond to the geometric mean computed by EHF10. The 'error bars' on the OUV data points represent the range of extinction corrections. Panel b (right): 1σ scatter around the average (model and observed) SEDs illustrating the diversity of individual SEDs. The solid line shows the average AD SED and the shaded region corresponds to the standard deviation from the AD models. The points correspond to the mean computed by EHF10 and the error bars show the scatter in the measurements. In the OUV, the filled circles correspond to measurements without any reddening correction whereas the open circles correspond to the maximal extinction correction.
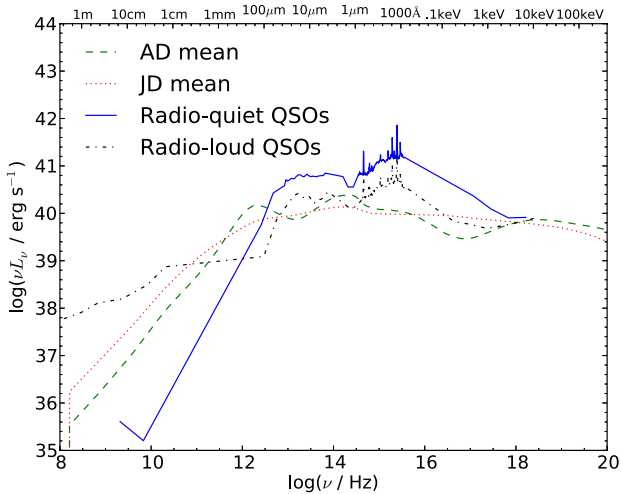
Figure 15. The average JD and AD model SEDs compared to the average radio-loud and radio-quiet quasar SEDs computed by Shang et al. (2011). All SEDs are normalized to the same 2–10 keV luminosity.

As expected, the average model SEDs agree well with the observed constraints. There are some details that are worth mentioning. The shape of the X-ray spectrum of the average JD SED is slightly softer than the corresponding shape of the average AD SED. Both are within the 1σ uncertainty in the photon index of the average observed SED. In the OUV, even though the model SEDs agree with the observed constraints they are quite different from each other. For instance, the red bump is stronger in the average AD SED. The average JD SED predicts a lower UV flux. In the radio band, the model SEDs are quite similar to each other.

Fig. 15 shows the average AD and JD SEDs compared to the average ones of radio-loud and radio-quiet quasars computed by Shang et al. (2011). The average quasar SEDs computed by Shang

et al. (2011) are very similar to the ones of Elvis et al. (1994) but the former include more detailed features and are based on more recent data obtained with improved instrumentation. As in Fig. 14(a), the SEDs were normalized such that they all have the same X-ray luminosity in the 2–10 keV band of 10^{40} erg s^{-1}. The UV excess in the quasar SEDs (the big blue bump) is clearly apparent in comparison to the LLAGN ones. It is also interesting that for $\nu > 10^{17}$ Hz the average AD, average JD and the radio-loud quasar SEDs are quite similar.

It is worth investigating how the luminosity is partitioned in different wavebands for the SEDs plotted in Fig. 15. For this purpose, we computed the luminosity contained in the radio (10^8–$10^{12.5}$ Hz), IR ($10^{12.5}$–$10^{14.5}$), OUV ($10^{14.5}$–$10^{16.5}$), X-rays (2–10 keV) and 'other' ($10^{16.5}$ Hz–2 keV and $E > 10$ keV) wavebands by integrating the SEDs, with the values in parenthesis denoting the range of frequencies or energies that we adopted for each waveband. The pie charts in Fig. 16 display the L_{band}/L_{bol} for each waveband defined above, for the average SEDs of LLAGNs and quasars. In the case of quasars, as is well known, the emission is dominated by the UV bump with the IR emission corresponding to the reprocessed emission of the accretion disc by the dust torus. In the case of the average AD and JD SEDs for the LLAGNs in our sample, the IR, OUV and 'other' bands release comparable fractions of the bolometric luminosity contrary to the case of quasars. In particular, the IR dominates the energy budget of the SED in the AD case. It is also notable that a higher fraction of the energy is released in the radio and X-rays compared to the quasar SEDs.

We remind the reader that the shape of the SEDs of individual objects may display a significant variance with respect to the average SEDs (e.g. Shang et al. 2011; Runnoe, Brotherton & Shang 2012; see also the discussion in Section 7.3). As such, although the energy budget displayed in Fig. 16 is an average representation of the whole sample of LLAGNs studied in our work and the Shang et al. quasar SEDs, it should be regarded with care when applied to individual sources.

LLAGNs (AD)

LLAGNs (JD)

Radio-loud quasars

Radio-quiet quasars
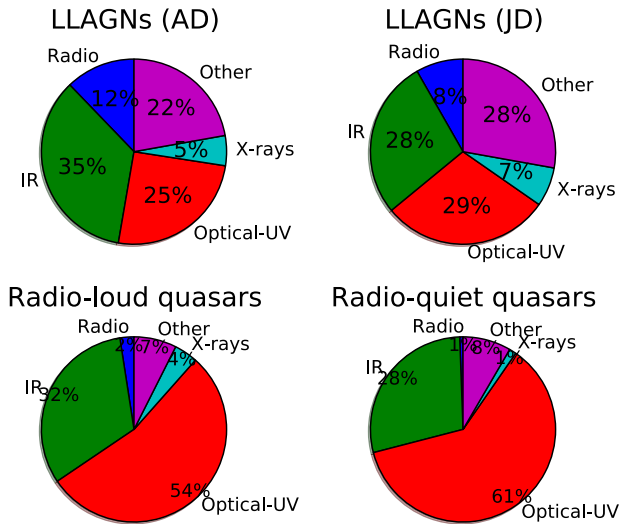
Figure 16. L_{band}/L_{bol} ratios for different wavebands, computed for the average AD and JD model SEDs, compared to the corresponding ratios for the average radio-loud and radio-quiet quasar SEDs of Shang et al. (2011). These average SEDs are displayed together in Fig. 15.

7 DISCUSSION

We discuss the caveats that affect our analysis in Section 7.1. In Section 7.2, we discuss the nature of X-rays in LLAGNs and in Section 7.5 we suggest directions for making progress in this issue.

7.1 Caveats

From an observational point of view, even though we are carrying one of the largest systematic analyses of the SEDs of LLAGNs to date (see also Wu et al. 2007; Yu et al. 2011), for most of the sources that we considered we only have a few data points available to fit. The lack of observational constraints, of course, impacts our ability to rule out the different scenarios for the central engine of LLAGNs – AD versus JD models – and to probe the transition between the ADAF and the thin disc. Therefore, it is clear that a strong case exists for obtaining more measurements and better detections of the sample over a broader range of wavelengths in order to better constrain the models for the central engine. We discuss specific observational strategies in Section 7.2. Furthermore, the size of our sample is limited. We need to extend our modelling to a larger number of LLAGNs in order to draw further conclusions.

From a theoretical perspective, there are considerable theoretical uncertainties involved in the ADAF–jet models. For instance, we cannot expect to constrain the ADAF parameters s and δ from the SED fitting since there is a degeneracy between these parameters (Quataert & Narayan 1999). Previous modelling efforts overcome the particular difficulty of the s/δ degeneracy by fixing the values of these parameters (e.g. Wu et al. 2007; Yuan et al. 2009) to the ones consistent with constraints from Sgr A* (Yuan et al. 2003). Despite recent progress (e.g. Sharma et al. 2007), the value of δ is essentially unconstrained. For this reason, the values of the parameters inferred in our fits do not correspond necessarily to unique choices but rather should be considered as illustrative of reasonable fits. Furthermore, our jet model is basically a phenomenological one: we have more freedom in the jet fitting compared to the ADAF model.

7.2 The nature of X-ray emission in LLAGNs

The nature of the X-ray emission in LLAGNs has been debated in the last few years by several authors favouring in some cases the AD or JD models based on the analysis of individual sources (e.g. Falcke & Markoff 2000; Yuan, Markoff & Falcke 2002a; Yuan et al. 2002b, 2003; Wu, Yuan & Cao 2007; Markoff et al. 2008; Miller et al. 2010) or in a statistical sense based on the Fundamental Plane of black hole activity (Merloni et al. 2003; Falcke et al. 2004; Yuan & Cui 2005; Yuan et al. 2009; Plotkin et al. 2012; Younes et al. 2012).

In our AD models, the X-rays are produced predominantly by inverse Compton scattering by the ADAF of seed synchrotron photons produced in the accretion flow itself; in contrast, in our JD models, the X-rays are dominated by the optically thin synchrotron emission at the base of the jet. In this regard, the X-ray spectrum is an important observable that can be used in order to disentangle the dominant component responsible for the LLAGNs. Internal shocks in the jet will favour electron energy distributions with power-law indices in the range $p \approx 2$–3 (Bednarz & Ostrowski 1998; Kirk et al. 2000; Achterberg et al. 2001; Sironi & Spitkovsky 2009). In the framework of JD models, the above range of values of p results in $\Gamma_X \approx 2$–2.5 (cf. Section 3.4). Therefore, sources characterized by X-ray spectra with $\Gamma_X \leq 2$ (i.e. on the hard side) are unlikely to be jet dominated in X-rays.

Fig. 17 illustrates the range of values of the X-ray photon index resulting from ADAFs with typical accretion rate as in the LLAGNs modelled in our sample. This figure demonstrates that ADAFs naturally accommodate hard X-ray emission with $\Gamma_X < 2$. In our sample, six LINERs have hard X-ray spectra which cannot be easily explained as jet emission whereas for only one source, NGC 4552, we were not able to find an AD model able to account for the soft X-ray SED with $\Gamma_X = 2$ (cf. Table 2).

Based on the observations above, we suggest that the spectral shape of the X-ray spectrum could be used to differentiate between an AD versus a JD origin for the X-rays. Namely, soft X-ray LLAGNs ($\Gamma_X \sim 2$–2.5) would be likely jet dominated whereas hard X-ray emitters ($\Gamma_X < 2$) would be ADAF dominated.

Note that it is still possible that relativistic shocks in jets could give rise to electron energy distributions with p slightly smaller than
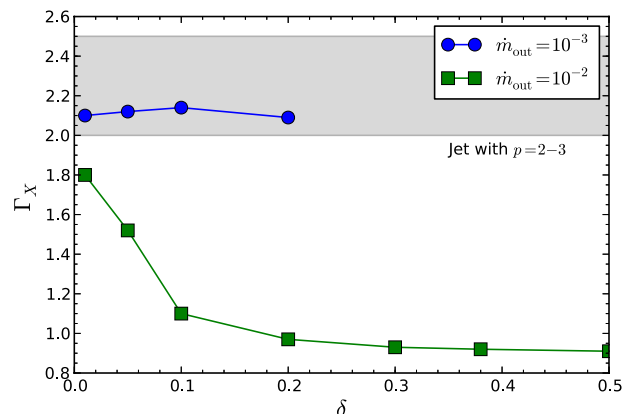
Figure 17. The X-ray photon index Γ_X predicted by ADAFs as a function of δ for different accretion rates. We computed Γ_X from a grid of ADAF models computed for $R_o = 500$, $s = 0.3$ and $m = 10^8$. The shaded region corresponds to the range of photon indices for jets with spectral index of the electron energy distribution in the range $p = 2$–3.

2 in a small fraction of sources (Starling et al. 2008; Curran et al. 2010) and, as noted by Yuan et al. (2009), reconnection effects could also change the electron energy distribution produced by shocks. In addition, ADAFs with relatively high accretion rates ($\dot{m}_o \approx 0.01$) can produce X-ray spectra with $\Gamma_X \approx 2.1$ (cf. Fig. 17) which has the same hardness as jets with $p = 2.2$. At these accretion rates, we expect that the thin disc would be truncated at radii $r_{tr} \sim 100$ (Yuan & Narayan 2004; Narayan & McClintock 2008) and hence the SED would be accompanied by relatively strong thermal emission in the near-IR. In the next section, we outline additional observations which will be crucial to disentangle the high-energy contribution of the jet and ADAF.

7.3 X-ray bolometric corrections in LLAGNs and quasars

It is instructive to compare the X-ray bolometric corrections we estimate in this work with those typical of quasars. One common way is to integrate the SED using the IR emission as a proxy of the intrinsic nuclear luminosity, assuming that a dust torus reprocesses the intrinsic OUV emission into IR radiation (e.g. Pozzi et al. 2007; Vasudevan et al. 2010; Lusso et al. 2011). Another closely related approach is to integrate the SED directly using the OUV emission (e.g. Marconi et al. 2004; Hopkins, Richards & Hernquist 2007; Vasudevan & Fabian 2007; Runnoe et al. 2012). For example, Lusso et al. (2011) find $\langle \kappa_X \rangle \sim 23$ for type I quasars whereas Runnoe et al. (2012) estimate $\langle \kappa_X \rangle \sim 38$ for their sample. An extrapolation of the results of Marconi et al. (2004) and Hopkins et al. (2007) to the luminosities characteristic of LLAGNs predicts values as low as 10 or even lower for κ_X (cf. also Vasudevan & Fabian 2007; Young, Elvis & Risaliti 2010; Lusso et al. 2011).

As we described in Section 5, we estimate L_{bol} by integrating the entire SED from radio up to 100 keV and including the IR emission since it is not clear at all whether the IR photons in LLAGNs should be treated as reprocessed emission from a dusty torus (e.g. Mason et al. 2013). We find $\kappa_X \approx 13 \left(L_X / 10^{41} \text{ erg s}^{-1} \right)^{-0.37}$ for the LLAGN SEDs in our sample; in other words, our average bolometric correction seems to be in rough agreement with the low values expected from the extrapolations of the quasar results mentioned above. At lower luminosities, our results suggest that κ_X increases slightly ($\kappa_X \approx 32$ at $L_X = 10^{40}$ erg s^{-1}).

We caution that extrapolations of bolometric corrections derived from quasar samples to lower luminosities have to be regarded with caution since, as we previously argued, it is likely that the accretion physics in LLAGNs may be significantly different compared to quasars. We also remind the reader that our κ_X estimates are subject to non-negligible uncertainties (~ 0.3 dex; cf. Section 5 and Appendix A) given the uncertainties in the L_{bol} determinations. In addition, the mean X-ray bolometric corrections can be inaccurate for individual objects due to variation in the X-ray emission and the SED shapes (or equivalently, the different degrees of contributions of the ADAF, thin disc and jet emission) from object to object, i.e. there is a large intrinsic scatter in the values of κ_X (cf. the scatter in the SEDs in Fig. 14b). Such a large scatter was also noted in the case of quasar SEDs (e.g. Marchese et al. 2012; Runnoe et al. 2012).

We now discuss a few individual sources and their associated X-ray bolometric corrections. Two examples of SEDs with relatively low κ_X correspond to the AD model for NGC 3998 (Fig. 4; $\kappa_X \approx 10$) and the JD model for NGC 4594 (Fig. 8; $\kappa_X \approx 11$). More generally, SEDs with $\kappa_X \lesssim 10$ are roughly flat (to first order) in the IR-to-X-ray range. On the other hand, many of the modelled SEDs in

our sample – in particular, the AD models – have considerable imbalances in the fraction of the luminosity radiated in the different wavebands. For instance, the integrated luminosity contained in the IR, OUV and >0.1 keV wavebands may considerably exceed L_X (see Fig. 16). For example, the models for NGC 1097 and NGC 4278 (κ_X values of 24 and 67, respectively) with their pronounced IR 'bumps' due to the truncated thin disc emission, and the extreme case of NGC 4143 with $\kappa_X \approx 146$.

7.4 The optical emission

The peak of the emission for a thin disc truncated at $r \sim 50-1000$ for $m \sim 10^8$ is typically located in the wavelength range $1-10\,\mu$m with a high-frequency tail extending into the optical and UV (e.g. Nemmen et al. 2006; Yu et al. 2011; Taam et al. 2012). Indeed, six sources (NGC 1097, NGC 3031, NGC 4143, NGC 4278, NGC 4374 and NGC 4736) display an OUV excess with respect to the ADAF and jet models. In four of these sources (NGC 1097, NGC 4143, NGC 4278 and NGC 4736), on the assumption that the OUV observations are dominated by the AGN, we were able to reproduce the data with the truncated thin disc emission with reasonable accretion rates and transition radii. For NGC 1097, NGC 3031 and NGC 4579 in particular, the transition radius is fixed by the modelling of the Hα double-peaked emission line (e.g. Storchi-Bergmann et al. 2003; Nemmen et al. 2006 and references therein); for these three LLAGNs, the thin disc component is significantly luminous (note that 4579 does not display an OUV excess with respect to the ADAF emission), given the relatively small transition radii implied by the Hα emission line. While the optical spectrum of NGC 1097 is explained by the thin disc emission, the available IR upper limits and OUV observations for NGC 3031 and NGC 4579 do not allow us to put useful constraints on the emission of the truncated thin disc for these sources. For the remaining sources in the sample, the lack of appropriate IR constraints – i.e. observations with high enough spatial resolution to accurately isolate the AGN – prevents us from better constraining the outer thin disc emission. We discuss observations that will be helpful in order to shed light into this issue in Section 7.5.

Even though the truncated thin disc is an appealing explanation for the OUV observations in many of the LINERs in our sample, we are unable to rule out the possibility that the optical emission in our sources is produced by an unresolved stellar population based solely on the SED modelling. This possibility was already pointed out by Maoz et al. (2005) and Maoz (2007). From the fits of stellar population models to the optical data, we obtained stellar masses in the range $\sim$a few 10^7–10^8 M$_\odot$ (Table 3). In fact, as we argued in Section 3.5, such an amount of mass due to unresolved stellar populations in the bulge within the *HST* aperture is quite feasible.

In addition, some of the galaxies in our sample could potentially host a compact nuclear star cluster, similarly to the Milky Way (Schödel, Merritt & Eckart 2009; Genzel et al. 2010). The compact nuclear star cluster in our Galaxy has a density $\rho_{NC} \sim 10^6$ M$_\odot$ pc^{-3} (Schödel et al. 2009; Genzel et al. 2010). If the galaxies in our sample host nuclear star clusters with similar densities as the Milky Way, then the implied star cluster mass enclosed within a radius R is

$$M_{NC} \sim 4 \times 10^9 \left(\frac{\rho_{NC}}{10^6 \text{ M}_\odot \text{ pc}^{-3}} \right) \left(\frac{R}{10 \text{ pc}} \right)^3 \text{ M}_\odot. \quad (5)$$

This mass estimate is likely to be on the high end for our sample; however, we do note that studies of galaxies hosting both nuclear

Table 3. Masses of stellar populations required to fit the *HST* optical emission for the galaxies in our sample.

Galaxy	Log mass ($M_\odot$)
NGC 1097	8.2
NGC 3031	7.8
NGC 3998	8.5
NGC 4143	7.7
NGC 4261	7.1
NGC 4278	8
NGC 4374	7.7
NGC 4486	8.3
NGC 4552	–
NGC 4579	8.1
NGC 4594	7.6
NGC 4736	8.1

star clusters and massive black holes suggest that the masses of these components are quite similar (Seth et al. 2008).

7.5 Future observational progress

We suggest different routes to clarify the issue of the nature of X-ray emission in LLAGNs in the future. The AD and JD models should predict different characteristic radio and X-ray variability time-scales (e.g. Ptak et al. 1998); hence, we should be able to test which component is dominant in X-rays by carrying out a simultaneous monitoring of the variability of radio and X-rays. By comparing the variability pattern predicted by jet/ADAF models, we could pinpoint the X-ray dominant component. This promising strategy is quite similar to what the observational campaigns carried out for M81 (Markoff et al. 2008; Miller et al. 2010) and could be applied to many other LLAGNs.

The *Fermi Gamma-ray Space Telescope* can be quite helpful in this regard. LLAGNs are potential sources of γ-rays (Takami 2011) and in fact one of the sources in this sample (NGC 4486) has already been detected by the *Fermi* Large Area Telescope (Abdo et al. 2009). By using the model parameters that we derived in our radio-to-X-ray fits, we should be able to predict the γ-ray spectrum (Mahadevan, Narayan & Krolik 1997; Takami 2011) and compare with future *Fermi* detections. In this way, we should be able to compare AD/JD predictions and through γ-ray observations place further constraints on the production site responsible for the high-energy emission and the jet–disc connection in LLAGNs.

Observations in the mm and sub-mm are also very helpful because they constrain the ADAF synchrotron emission and hence also the X-ray emission. This follows because the synchrotron photons in the ADAF are inverse Compton scattered to X-rays.

Another future direction for a shedding light on the role of the jet in the SEDs of LLAGNs lies in refining and better understanding of the Fundamental Plane of black hole activity (Merloni et al. 2003; Falcke et al. 2004; Gültekin et al. 2009; Yuan et al. 2009; Plotkin et al. 2012) as a tool for constraining the radiative processes shaping the radio and X-ray emission in sub-Eddington black hole sources.

Finally, it is crucial to observe the LLAGNs of our sample at high spatial resolution in the IR wavebands in order to probe the presence of the outer thin disc component. There has been recent observational progress on this front (Asmus et al. 2011; Fernández-Ontiveros et al. 2012; Mason et al. 2012). Since emission from hot dust is also important in these IR bands, the contribution of

the putative dusty torus (Ramos Almeida et al. 2011) must also be taken into account. Modelling these recent observations is beyond the scope of this work (cf. Mason et al., 2013).

8 SUMMARY

We performed a detailed exploratory modelling of the broad-band SEDs of a sample of 12 LLAGNs in LINERs selected from EHF10 based on the presence of compact radio cores and nuclear X-ray point sources as well as the availability of high-resolution optical/UV observations. Our coupled accretion-jet model consists of an accretion flow which is radiatively inefficient in the inner parts and becomes a thin disc outside a certain transition radius. The relativistic jet is modelled in the framework of the internal shock scenario. In the framework of our model, our main results are as follows.

(i) We find that there are two broad classes of models that can explain the majority of the observed SEDs. We call the first one AD which stands for 'ADAF dominated' since the ADAF dominates most of the broad-band emission, particularly in X-rays. In the second class of models, the jet component dominates the majority of the continuum emission and for this reason we call this scenario JD as in 'jet dominated'.

(ii) We suggest that the spectral shape of the X-ray spectrum could be used to differentiate between an AD versus a JD origin for the X-rays: soft X-ray LLAGNs (photon spectral indices $\sim$2–2.5) are likely jet dominated whereas hard X-ray emitters (photon indices <2) are likely ADAF dominated. We discuss different observational strategies to make progress in understanding the origin of X-rays in LLAGNs.

(iii) The radio band is almost always dominated by the synchrotron emission from the jet, confirming previous results.

(iv) Six sources in our sample display an OUV excess with respect to ADAF and jet models; in four of them (NGC 1097, NGC 4143, NGC 4278 and NGC 4736), this excess can be reproduced by emission from a truncated thin accretion disc with transition radii in the range 30–225R_S. Alternatively, unresolved, old stellar populations with masses $\sim 10^7$–10^8 $M_\odot$ located within $\approx$2–15 pc of the nuclei can also reproduce the *HST* optical observations.

(v) The mass accretion rates that reach the outer radius of the ADAF – based on the AD models – lie in the range $\sim 1 \times 10^{-4}$–0.02 in Eddington units. These accretion rates are likely to represent upper limits if the jet is the dominant contributor to the broad-band high-energy emission.

(vi) Typically $\sim$10 per cent of these accretion rates reach 3R_S with the remaining gas being presumably lost due to outflows.

(vii) The efficiency of conversion of the rest mass energy associated with gas supplied to the accretion flow into disc+jet radiation is in the range $\sim(10^{-3}$–0.1) per cent.

(viii) Jet kinetic powers from the SED models are in the range $\sim 10^{40}$–10^{44} erg s^{-1}. The efficiency with which the rest mass energy associated with gas supplied to the black hole is converted into jet kinetic power is in the range 0.1–10 per cent.

(ix) We find hints of correlations between the accretion rate and jet power (2σ) and anticorrelation ($\approx$1.6σ) between the radio loudness – estimated using the core radio luminosity – and the accretion rate.

(x) We compute the average SED for LLAGNs using our model fits. The average SEDs are quite different from the quasar ones and display a slight IR bump. High spatial resolution IR observations are required in order to better constrain the physics of IR emission in LLAGNs.

(xi) There is evidence for a non-linear relation between the 2–10 keV and the bolometric luminosity for the sources in our sample [$\log L_{\rm bol} = (0.63 \pm 0.12) \log L_{\rm X} + 16.3 \pm 4.9$].

This work highlights the need for a better multiwavelength coverage of LLAGN SEDs in order to make progress in understanding the role of the different components of the central engine. The individual and average SED models that we computed can be useful for a number of different applications.

ACKNOWLEDGEMENTS

REFERENCES

Abdo A. A. et al., 2009, ApJ, 707, 55
Achterberg A., Gallant Y. A., Kirk J. G., Guthmann A. W., 2001, MNRAS, 328, 393
Akritas M. G., Bershady M. A., 1996, ApJ, 470, 706
Allen S. W., Dunn R. J. H., Fabian A. C., Taylor G. B., Reynolds C. S., 2006, MNRAS, 372, 21
Asmus D., Gandhi P., Smette A., Hönig S. F., Duschl W. J., 2011, A&A, 536, A36
Balmaverde B., Baldi R. D., Capetti A., 2008, A&A, 486, 119
Barth A. J., Ho L. C., Filippenko A. V., Rix H.-W., Sargent W. L. W., 2001, ApJ, 546, 205
Bednarz J., Ostrowski M., 1998, Phys. Rev. Lett., 80, 3911
Begelman M. C., 2012, MNRAS, 420, 2912
Bicknell G. V., Begelman M. C., 1999, in Röser H.-J., Meisenheimer K., eds, Lecture Notes in Physics, Vol. 530, The Radio Galaxy Messier 87. Springer-Verlag, Berlin, p. 235
Bietenholz M. F., Bartel N., Rupen M. P., 2000, ApJ, 532, 895
Biretta J. A., Sparks W. B., Macchetto F., 1999, ApJ, 520, 621
Blandford R. D., Begelman M. C., 1999, MNRAS, 303, L1
Bower G. A. et al., 2000, ApJ, 534, 189
Broderick J. W., Fender R. P., 2011, MNRAS, 417, 184
Bruzual G., Charlot S., 2003, MNRAS, 344, 1000
Chen K., Halpern J. P., 1989, ApJ, 344, 115
Chen K., Halpern J. P., Filippenko A. V., 1989, ApJ, 339, 742
Curran P. A., Evans P. A., de Pasquale M., Page M. J., van der Horst A. J., 2010, ApJ, 716, L135
David L. P., Jones C., Forman W., Murray S. S., 2005, ApJ, 635, 1053
De Villiers J.-P., Hawley J. F., Krolik J. H., 2003, ApJ, 599, 1238
Devereux N., 2011, ApJ, 727, 93
Devereux N., Shearer A., 2007, ApJ, 671, 118
Devereux N., Ford H., Tsvetanov Z., Jacoby G., 2003, AJ, 125, 1226
Di Matteo T., Carilli C. L., Fabian A. C., 2001, ApJ, 547, 731

Di Matteo T., Allen S. W., Fabian A. C., Wilson A. S., Young A. J., 2003, ApJ, 582, 133
Done C., Gierliński M., Kubota A., 2007, A&AR, 15, 1
Elvis M. et al., 1994, ApJS, 95, 1
Eracleous M., Shields J. C., Chartas G., Moran E. C., 2002, ApJ, 565, 108
Eracleous M., Lewis K. T., Flohic H. M. L. G., 2009, New Astron. Rev., 53, 133
Eracleous M., Hwang J. A., Flohic H. M. L. G., 2010a, ApJS, 187, 135 (EHF10)
Eracleous M., Hwang J. A., Flohic H. M. L. G., 2010b, ApJ, 711, 796
Falcke H., Markoff S., 2000, A&A, 362, 113
Falcke H., Körding E., Markoff S., 2004, A&A, 414, 895
Fernández-Ontiveros J. A., Prieto M. A., Acosta-Pulido J. A., Montes M., 2012, J. Phys.: Conf. Ser., 372, 012006
Ferrarese L., Merritt D., 2000, ApJ, 539, L9
Finoguenov A., Ruszkowski M., Jones C., Brüggen M., Vikhlinin A., Mandel E., 2008, ApJ, 686, 911
Frank J., King A., Raine D. J., 2002, Accretion Power in Astrophysics, 3rd edn. Cambridge Univ. Press, Cambridge
Freedman W. L. et al., 1994, ApJ, 427, 628
Freedman W. L. et al., 2001, ApJ, 553, 47
Gavazzi G., Boselli A., Scodeggio M., Pierini D., Belsole E., 1999, MNRAS, 304, 595
Gebhardt K., Thomas J., 2009, ApJ, 700, 1690
Gebhardt K. et al., 2000, ApJ, 539, L13
Genzel R., Eisenhauer F., Gillessen S., 2010, Rev. Mod. Phys., 82, 3121
Giroletti M., Taylor G. B., Giovannini G., 2005, ApJ, 622, 178
Gliozzi M., Sambruna R. M., Brandt W. N., 2003, A&A, 408, 949
Gültekin K., Cackett E. M., Miller J. M., Di Matteo T., Markoff S., Richstone D. O., 2009, ApJ, 706, 404
Hawley J. F., Krolik J. H., 2001, ApJ, 548, 348
Hawley J. F., Krolik J. H., 2006, ApJ, 641, 103
Heckman T. M., 1980, A&A, 87, 152
Heinz S., Merloni A., Schwab J., 2007, ApJ, 658, L9
Ho L. C., 1999, ApJ, 516, 672
Ho L. C., 2002, ApJ, 564, 120
Ho L. C., 2008, ARA&A, 46, 475
Ho L. C., 2009, ApJ, 699, 626
Ho L. C., Peng C. Y., 2001, ApJ, 555, 650
Ho L. C., Filippenko A. V., Sargent W. L., 1995, ApJS, 98, 477
Ho L. C., Filippenko A. V., Sargent W. L. W., 1997a, ApJS, 112, 315
Ho L. C., Filippenko A. V., Sargent W. L. W., 1997b, ApJ, 487, 568
Hopkins P. F., Hernquist L., 2006, ApJS, 166, 1
Hopkins P. F., Narayan R., Hernquist L., 2006, ApJ, 643, 641
Hopkins P. F., Richards G. T., Hernquist L., 2007, ApJ, 654, 731
Igumenshchev I. V., Narayan R., Abramowicz M. A., 2003, ApJ, 592, 1042
Jensen J. B., Tonry J. L., Barris B. J., Thompson R. I., Liu M. C., Rieke M. J., Ajhar E. A., Blakeslee J. P., 2003, ApJ, 583, 712
Kato S., Fukue J., Mineshige S., eds, 1998, Black-Hole Accretion Disks. Kyoto Univ. Press, Kyoto, Japan
Kellermann K. I., Sramek R., Schmidt M., Shaffer D. B., Green R., 1989, AJ, 98, 1195
Kirk J. G., Guthmann A. W., Gallant Y. A., Achterberg A., 2000, ApJ, 542, 235
Kormendy J., Kennicutt R. C., Jr, 2004, ARA&A, 42, 603
Lasota J.-P., Abramowicz M. A., Chen X., Krolik J., Narayan R., Yi I., 1996, ApJ, 462, 142
Lemoine M., Pelletier G., 2003, ApJ, 589, L73
Li Y.-R., Yuan Y.-F., Wang J.-M., Wang J.-C., Zhang S., 2009, ApJ, 699, 513
Liu H., Wu Q., 2013, ApJ, 764, 17
Lusso E. et al., 2011, A&A, 534, A110
Mahadevan R., Narayan R., Krolik J., 1997, ApJ, 486, 268
Manmoto T., Kato S., Nakamura K. E., Narayan R., 2000, ApJ, 529, 127
Maoz D., 2007, MNRAS, 377, 1696
Maoz D., Koratkar A., Shields J. C., Ho L. C., Filippenko A. V., Sternberg A., 1998, AJ, 116, 55
Maoz D., Nagar N. M., Falcke H., Wilson A. S., 2005, ApJ, 625, 699

Marchese E., Della Ceca R., Caccianiga A., Severgnini P., Corral A., Fanali R., 2012, A&A, 539, A48

Marconi A., Risaliti G., Gilli R., Hunt L. K., Maiolino R., Salvati M., 2004, MNRAS, 351, 169

Markoff S. et al., 2008, ApJ, 681, 905

Marrone D. P., Moran J. M., Zhao J.-H., Rao R., 2007, ApJ, 654, L57

Mason R. E. et al., 2012, AJ, 144, 11

Mason R. E., Ramos Almeida C., Levenson N. A., Nemmen R., Alonso-Herrero A., 2013, ApJ, 777, 164

McKinney J. C., Gammie C. F., 2004, ApJ, 611, 977

McKinney J. C., Tchekhovskoy A., Blandford R. D., 2012, MNRAS, 423, 3083

Merloni A., Heinz S., 2007, MNRAS, 381, 589

Merloni A., Heinz S., 2008, MNRAS, 388, 1011

Merloni A., Heinz S., di Matteo T., 2003, MNRAS, 345, 1057

Miller J. M., Nowak M., Markoff S., Rupen M. P., Maitra D., 2010, ApJ, 720, 1033

Nagar N. M., Falcke H., Wilson A. S., Ho L. C., 2000, ApJ, 542, 186

Nagar N. M., Wilson A. S., Falcke H., 2001, ApJ, 559, L87

Nagar N. M., Falcke H., Wilson A. S., 2005, A&A, 435, 521

Narayan R., McClintock J. E., 2008, New Astron. Rev., 51, 733

Narayan R., Yi I., 1994, ApJ, 428, L13

Narayan R., Yi I., 1995, ApJ, 452, 710

Narayan R., Mahadevan R., Quataert E., 1998, in Abramowicz M. A., Bjornsson G., Pringle J. E., eds, Theory of Black Hole Accretion Disks. Cambridge Univ. Press, Cambridge, p. 148

Narayan R., Igumenshchev I. V., Abramowicz M. A., 2000, ApJ, 539, 798

Narayan R., Sadowski A., Penna R. F., Kulkarni A. K., 2012, MNRAS, 426, 3241

Nemmen R. S., Storchi-Bergmann T., Yuan F., Eracleous M., Terashima Y., Wilson A. S., 2006, ApJ, 643, 652

Nemmen R. S., Bower R. G., Babul A., Storchi-Bergmann T., 2007, MNRAS, 377, 1652

Nemmen R. S., Georganopoulos M., Guiriec S., Meyer E. T., Gehrels N., Sambruna R. M., 2012, Science, 338, 1445

Owen F. N., Eilek J. A., Kassim N. E., 2000, ApJ, 543, 611

Pellegrini S., 2005, ApJ, 624, 155

Piran T., 1999, Phys. Rep., 314, 575

Plotkin R. M., Markoff S., Kelly B. C., Körding E., Anderson S. F., 2012, MNRAS, 419, 267

Pozzi F. et al., 2007, A&A, 468, 603

Proga D., Begelman M. C., 2003, ApJ, 592, 767

Ptak A., Yaqoob T., Mushotzky R., Serlemitsos P., Griffiths R., 1998, ApJ, 501, L37

Ptak A., Terashima Y., Ho L. C., Quataert E., 2004, ApJ, 606, 173

Quataert E., Gruzinov A., 1999, ApJ, 520, 248

Quataert E., Narayan R., 1999, ApJ, 520, 298

Quataert E., Di Matteo T., Narayan R., Ho L. C., 1999, ApJ, 525, L89

Ramos Almeida C. et al., 2011, ApJ, 731, 92

Remillard R. A., McClintock J. E., 2006, ARA&A, 44, 49

Runnoe J. C., Brotherton M. S., Shang Z., 2012, MNRAS, 422, 478

Russell H. R., McNamara B. R., Edge A. C., Hogan M. T., Main R. A., Vantyghem A. N., 2013, MNRAS, 432, 530

Sarzi M. et al., 2010, MNRAS, 402, 2187

Schödel R., Merritt D., Eckart A., 2009, A&A, 502, 91

Seth A., Agüeros M., Lee D., Basu-Zych A., 2008, ApJ, 678, 116

Shang Z. et al., 2011, ApJS, 196, 2

Sharma P., Quataert E., Hammett G. W., Stone J. M., 2007, ApJ, 667, 714

Shcherbakov R. V., Penna R. F., McKinney J. C., 2012, ApJ, 755, 133

Sijacki D., Springel V., Di Matteo T., Hernquist L., 2007, MNRAS, 380, 877

Sikora M., Stawarz Ł., Lasota J.-P., 2007, ApJ, 658, 815

Singh R. et al., 2013, A&A, 558, A43

Sironi L., Spitkovsky A., 2009, ApJ, 698, 1523

Soria R., Fabbiano G., Graham A. W., Baldi A., Elvis M., Jerjen H., Pellegrini S., Siemiginowska A., 2006a, ApJ, 640, 126

Soria R., Graham A. W., Fabbiano G., Baldi A., Elvis M., Jerjen H., Pellegrini S., Siemiginowska A., 2006b, ApJ, 640, 143

Spada M., Ghisellini G., Lazzati D., Celotti A., 2001, MNRAS, 325, 1559

Starling R. L. C., van der Horst A. J., Rol E., Wijers R. A. M. J., Kouveliotou C., Wiersema K., Curran P. A., Weltevrede P., 2008, ApJ, 672, 433

Steffen A. T., Strateva I., Brandt W. N., Alexander D. M., Koekemoer A. M., Lehmer B. D., Schneider D. P., Vignali C., 2006, AJ, 131, 2826

Stone J. M., Pringle J. E., 2001, MNRAS, 322, 461

Storchi-Bergmann T. et al., 2003, ApJ, 598, 956

Storchi-Bergmann T., Nemmen R. S., Spinelli P. F., Eracleous M., Wilson A. S., Filippenko A. V., Livio M., 2005, ApJ, 624, L13

Taam R. E., Liu B. F., Yuan W., Qiao E., 2012, ApJ, 759, 65

Takami H., 2011, MNRAS, 413, 1845

Tchekhovskoy A., Narayan R., McKinney J. C., 2011, MNRAS, 418, L79

Terashima Y., Wilson A. S., 2003, ApJ, 583, 145

Terashima Y., Iyomoto N., Ho L. C., Ptak A. F., 2002, ApJS, 139, 1

Tonry J. L., Dressler A., Blakeslee J. P., Ajhar E. A., Fletcher A. B., Luppino G. A., Metzger M. R., Moore C. B., 2001, ApJ, 546, 681

Tremaine S. et al., 2002, ApJ, 574, 740

Tully R. B., Fisher J. R., 1988, Catalog of Nearby Galaxies. Cambridge Univ. Press, Cambridge

Ulvestad J. S., Ho L. C., 2001, ApJ, 562, L133

Vasudevan R. V., Fabian A. C., 2007, MNRAS, 381, 1235

Vasudevan R. V., Fabian A. C., Gandhi P., Winter L. M., Mushotzky R. F., 2010, MNRAS, 402, 1081

Wang Q. D. et al., 2013, Science, 341, 981

Wong K.-W., Irwin J. A., Yukita M., Million E. T., Mathews W. G., Bregman J. N., 2011, ApJ, 736, L23

Wu Q., Cao X., 2005, ApJ, 621, 130

Wu Q., Yuan F., Cao X., 2007, ApJ, 669, 96

Wu Q., Yan H., Yi Z., 2013, MNRAS, 436, 1278

Wyse R. F. G., Gilmore G., Franx M., 1997, ARA&A, 35, 637

Xie F.-G., Yuan F., 2012, MNRAS, 427, 1580

Xu Y.-D., Cao X., 2010, ApJ, 716, 1423

Yan R., Blanton M. R., 2012, ApJ, 747, 61

Younes G., Porquet D., Sabra B., Reeves J. N., Grosso N., 2012, A&A, 539, A104

Young M., Elvis M., Risaliti G., 2009, ApJS, 183, 17

Young M., Elvis M., Risaliti G., 2010, ApJ, 708, 1388

Yu Z., Yuan F., Ho L. C., 2011, ApJ, 726, 87

Yuan F., 2007, in Ho L. C., Wang J.-W., eds, ASP Conf. Ser. Vol. 373, The Central Engine of Active Galactic Nuclei. Astron. Soc. Pac., San Francisco, p. 95

Yuan F., Cui W., 2005, ApJ, 629, 408

Yuan F., Narayan R., 2004, ApJ, 612, 724

Yuan F., Peng Q., Lu J.-f., Wang J., 2000, ApJ, 537, 236

Yuan F., Markoff S., Falcke H., 2002a, A&A, 383, 854

Yuan F., Markoff S., Falcke H., Biermann P. L., 2002b, A&A, 391, 139

Yuan F., Quataert E., Narayan R., 2003, ApJ, 598, 301

Yuan F., Cui W., Narayan R., 2005, ApJ, 620, 905

Yuan F., Shen Z.-Q., Huang L., 2006, ApJ, 642, L45

Yuan F., Ma R., Narayan R., 2008, ApJ, 679, 984

Yuan F., Yu Z., Ho L. C., 2009, ApJ, 703, 1034

Yuan F., Bu D., Wu M., 2012, ApJ, 761, 130

APPENDIX A: UNCERTAINTIES IN DERIVED PARAMETERS OF LLAGNS

In this section, we estimate the uncertainties in the main parameters obtained from the SED models such as mass accretion rates and jet powers.

(1) *Accretion rate*. In order to estimate the uncertainty in $\dot{m}$ from the AD models, we assume that the bolometric luminosity of LLAGNs can be approximated as the ADAF total luminosity, $L_{bol} \sim L_{adaf}$. We note that this may not be a good approximation for systems in which the thin disc is truncated at low radii, since in such situations the truncated disc can contribute a significant part of the luminosity. Correspondingly, for LLAGNs in which the emission

is dominated by the jet, this approximation is also not appropriate. We use the fitting formulae for the ADAF radiative efficiencies computed by Xie & Yuan (2012) for different values of δ, assuming $s = 0.4$ and $R_o = 100$ (cf. their table 1). We evaluate how much $\dot{m}_o$ varies by changing the value of δ between 10^{-3} and 0.5, for $L_{bol} = $ const. We find that $\dot{m}_o$ is affected by a systematic uncertainty of 0.2 dex due to our uncertain knowledge of the value of δ.

The above estimate is appropriate for fixed values of s and R_o. It is possible that ADAFs have systematically different amounts of mass-loss due to outflows or convection than what we considered (e.g. Shcherbakov, Penna & McKinney 2012). If this is the case, then our values of $\dot{m}$ could be biased towards higher rates if $s > 0.3$ and lower rates if $s < 0.3$ (the fiducial value of s that we adopted in our SED models). In order to estimate the degree to which different values of s could affect the estimated accretion rates, we computed a grid of ADAF SED models for $R_o = 10^4$, $\delta = 0.1$, $m = 10^8$ and $\alpha = 0.3$ for which we varied the accretion rates and the values of s in the ranges $\dot{m}_o = 10^{-4}-0.01$ and $s = 0.1-0.5$. By considering how much the accretion rate varies in order to reproduce a fixed value of L_{bol}, we estimate rough uncertainties in $\dot{m}_o$ of a factor of 5 in each direction (0.7 dex; slightly smaller for smaller values of R_o).

Combining the above uncertainties in quadrature with the systematic scatter of 0.23 dex resulting from the $M-\sigma$ relation (Tremaine et al. 2002), we estimate a systematic uncertainty in $\dot{m}_o$ of ~0.8 dex (keeping in mind that this is a rough estimate since s and δ should be correlated). The uncertainty in the 'Bondi accretion power' P_{Bondi} as defined in the main text is estimated to be of the same order.

We expect that the uncertainty in the accretion rate due to our lack of understanding in the structure of ADAFs (values of s and δ) and the uncertainty in the black hole mass will dominate over the observational sources of uncertainty (i.e. error in the observed fluxes, paucity of SED sampling in some sources).

(2) *Bolometric luminosity.* The bolometric luminosities and Eddington ratios for the LINERs in our sample are affected by a factor of 5 (~0.7 dex) uncertainties according to the estimate of EHF10. Correspondingly, the typical uncertainty in η_{rad} is ~0.8 dex. The typical relative uncertainty in the X-ray luminosities was estimated by EHF10 as $\sigma L_X/L_X \approx 0.2$ which corresponds to ≈0.1 dex.

(3) *Jet power.* In order to estimate the uncertainty in the jet powers derived from the SED models, we consider for illustration how the relativistic jet model (Section 3.3) reproduces the radio spectrum of NGC 4594. By fixing $\epsilon_e = 0.1$ and $\epsilon_B = 0.01$, we consider two values of the bulk Lorentz factor, 2.3 (the fiducial one) and 7 as suggested by Merloni & Heinz (2007), and vary $\dot{m}_{jet}$ in order to fit the radio SED. The uncertainty in the value of Γ_j results in a factor of 5 systematic uncertainty in P_{jet}, similarly to the uncertainty affecting L_{bol}. The uncertainty in P_{jet}/L_{Edd} corresponds to ~0.76 dex. The uncertainty affecting the jet kinetic efficiency should be of the same order of magnitude as the one affecting P_{jet}/L_{Edd}.

(4) *Radio loudness.* The uncertainty in the radio loudness depends on the corresponding errors affecting the radio and optical luminosities. We estimate that the typical uncertainties in $L_\nu(6\,cm)$ and $L_\nu(4400\,\text{Å})$ correspond to ~0.1 and ~0.5 dex, respectively. The latter error is due to the uncertain amount of intrinsic extinction. Therefore, our R_o estimates have an ~0.5 dex uncertainty.

APPENDIX B: FITS TO SPARSELY SAMPLED SEDs

We present in this section the model fits to the nine SEDs that, although displaying nuclear X-ray point sources observed with *Chan-*
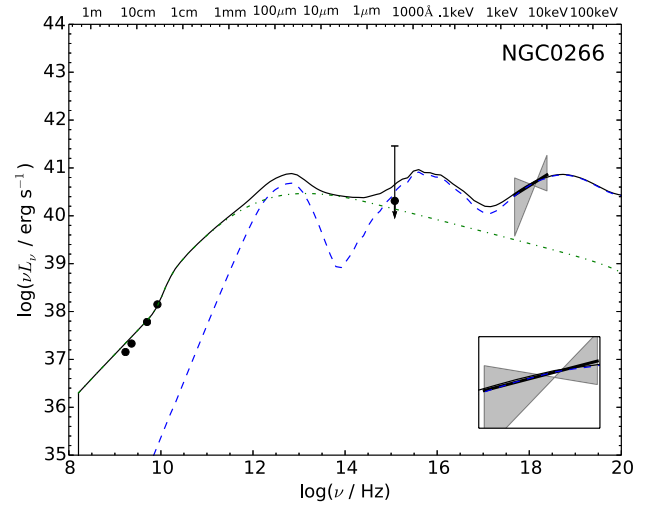
Figure B1. The SED and ADAF-dominated model for NGC 266. The dashed, dotted and dot–dashed lines correspond to the emission from the ADAF, truncated thin disc and jet, respectively. The solid line represents the sum of the emission from all components. The inset shows the zoomed 2–10 keV spectrum.
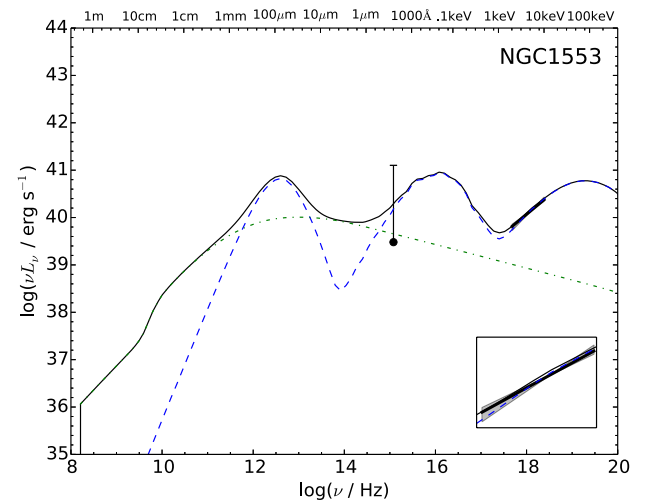

Figure B2. Same as Fig. B1 for NGC 1553.

dra, did not pass the quality cut discussed in Section 2 for lacking a radio core or *HST* optical/UV observations but nevertheless have estimates of the black hole mass and X-ray SEDs available.

The SED fits are shown in Figs B1–B5. In the subsections below, we briefly describe the details of the fits to the SED of each object. The basic properties of the LLAGNs and the model parameters are summarized in Tables B1 and B2, respectively.

B1 NGC 0266

The AD model accounts slightly better for the best-fitting X-ray slope, but note the pronounced uncertainty on the value of observed photon index. The JD model requires $p < 2$ which is below the usual range $2 < p < 3$ suggested by relativistic shock theory (Bednarz & Ostrowski 1998; Kirk et al. 2000) and hence is disfavoured (Fig. B1).
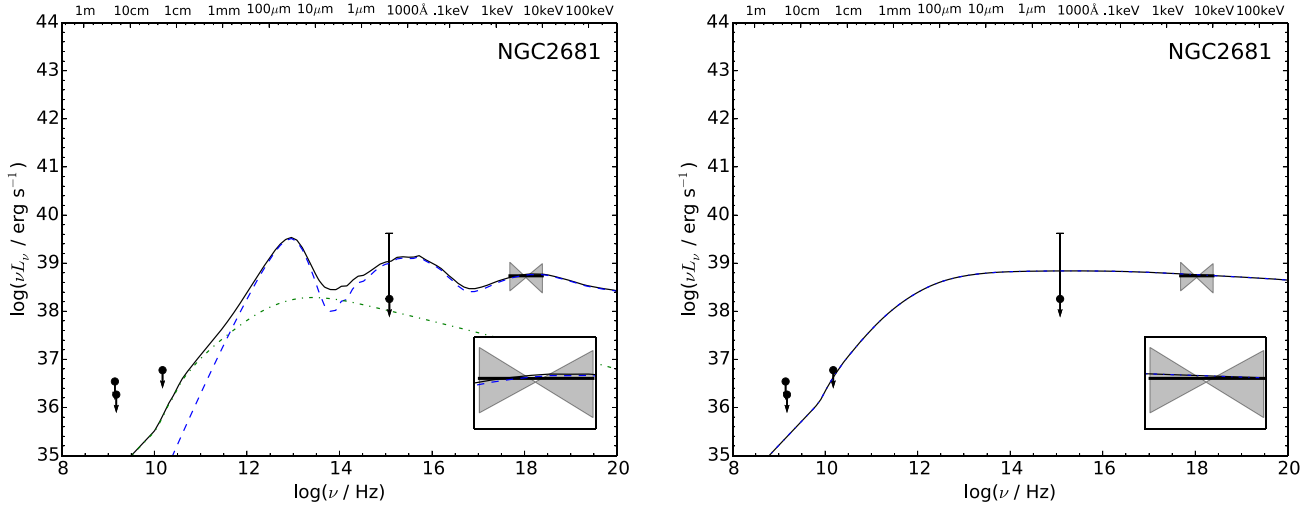
Figure B3. SEDs and coupled accretion–jet models for NGC 1553. The left-hand panel shows the AD models for each object while the right-hand panel displays the JD models.

B2 NGC 1553

The Bondi accretion rate was estimated by Pellegrini (2005). Even though the JD model roughly accounts for the estimated L_X, it fails to fit the slope of the X-ray spectrum even with a small value of p. We take this as evidence that this source is unlikely to be JD (Fig. B2). The estimated $\dot{m}_o$ is consistent with the lower limit on $\dot{m}_{Bondi}$ obtained by Pellegrini (2005).

B3 NGC 2681

For this LLAGN, there are not enough optical observations to fit the truncated thin disc model and estimate the transition radius (Fig. B3).

B4 NGC 3169

As was the case of NGC 2681, for this LLAGN there are not enough optical observations to fit the truncated thin disc model and estimate the transition radius. The JD model accounts well for the available data. The inferred extreme values of ϵ_e and ϵ_B imply that essentially all the energy in the post-shock region of the jet is carried by the particles.

B5 NGC 3226

The SED of this LLAGN is well fitted by both an AD and a JD type of models. As is the case of NGC 2681, there are no good optical band constraints on the emission of the truncated thin disc.

B6 NGC 3379

This source has only two data points outside the X-ray band, one in the radio and the other in the optical, both of which correspond to upper limits. Therefore, there are few constraints for the accretion-jet model. The Bondi rate was estimated by David et al. (2005).

The AD model is able to reproduce the observed SED given the few constraints available, but there are no radio data to constrain the jet model in this case so we do not include it. The available data are not enough to constrain well the transition radius. The accretion rate required by the AD model is more than an order of magnitude higher than $\dot{m}_{Bondi}$. One possible explanation for this result is that the accretion rate is enhanced by gas released by stars. This is in line with the findings of Soria et al. (2006a,b) for a sample of quiescent early-type galaxies.

B7 NGC 4457

Since there are only upper limits in the radio band, the jet power for this object was estimated using the observation at $\nu = 1.5 \times 10^{10}$ Hz and the Merloni & Heinz (2007) correlation.

B8 NGC 4494

Same as NGC 4457.

B9 NGC 4548

Same as NGC 4457. Given the large uncertainty in the photon index, the X-ray spectrum does not provide good constraints for the models.
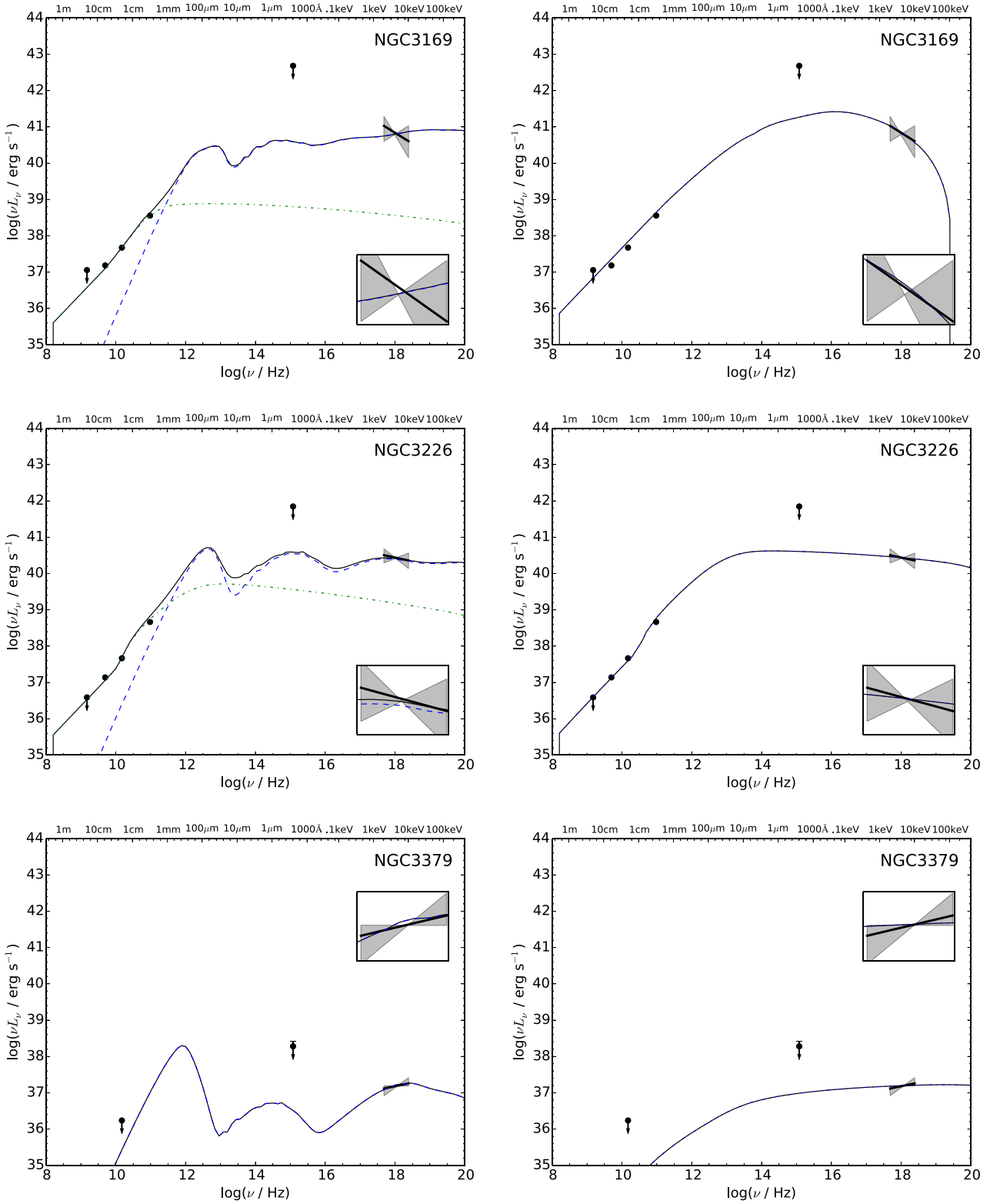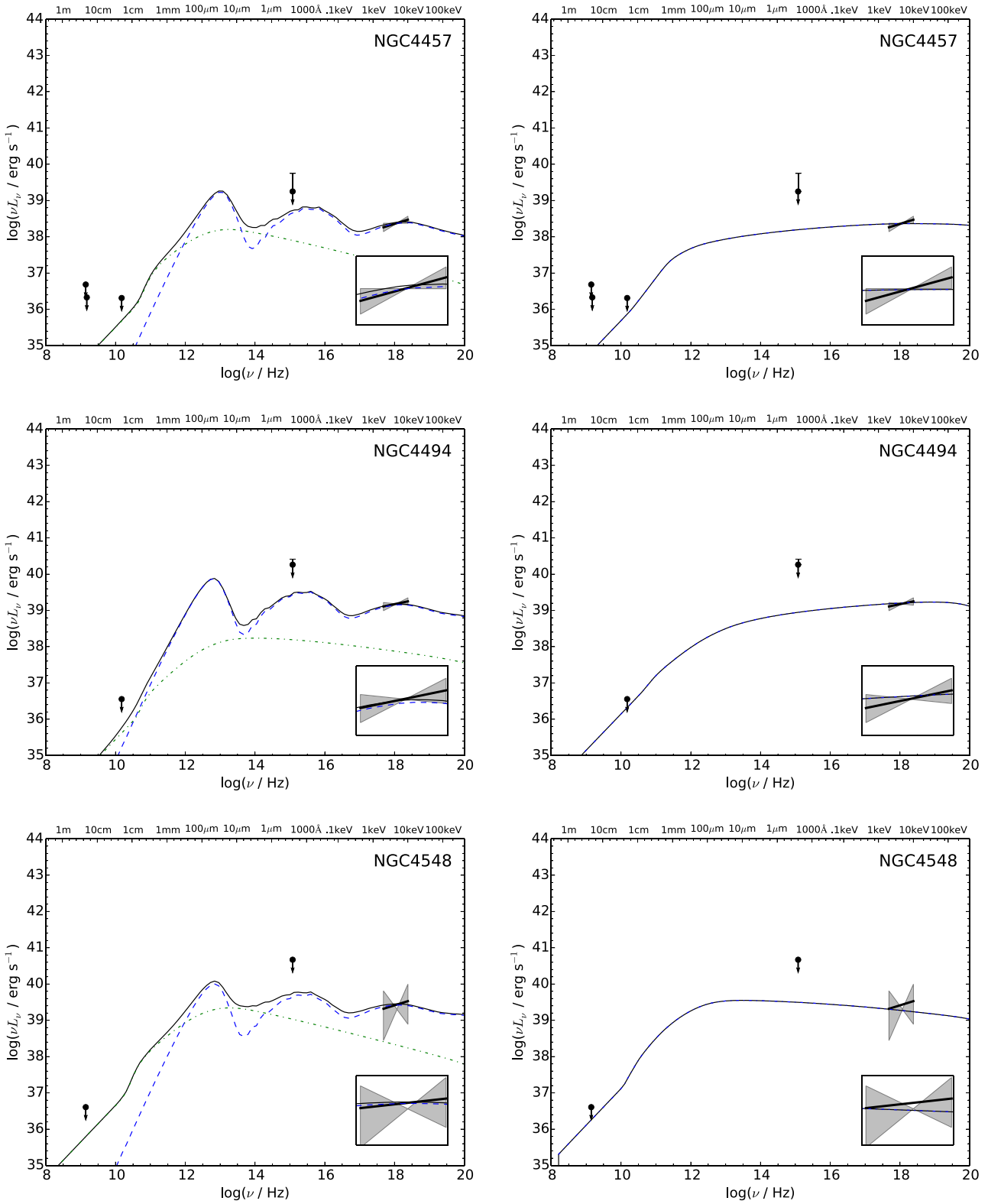
Figure B4. Same as Fig. 3 for NGC 2681, NGC 3169 and NGC 3226.

Figure B5. Same as Fig. 3 for NGC 4278, NGC 4457 and NGC 4494.

Table B1. Sample of galaxies with sparsely sampled SEDs and their basic properties. Notation is the same as in Table 1.

Galaxy	Hubble type	Distance[a] (Mpc)	log ($M_{BH}/M_{\odot}$)	LINER type	L_X (erg s^{-1})[b]	L_{bol} (erg s^{-1})[c]	L_{bol}/L_{Edd}
NGC 266	SB(rs)ab	62.4 (1)	7.6[d]	L1	7.4×10^{40}	2.2×10^{42}	4×10^{-4}
NGC 2681	SBA(rs)0/a	16.0 (2)	7.1	L1	6.1×10^{38}	1.8×10^{40}	1×10^{-5}
NGC 3169	SA(s)a	19.7 (1)	7.8	L2	1.1×10^{41}	3.3×10^{42}	4×10^{-4}
NGC 3226	E2	21.9 (2)	8.1	L1	5.0×10^{40}	1.5×10^{42}	1×10^{-4}
NGC 3379	E1	9.8 (2)	8.2	L2/T2	1.7×10^{37}	5.1×10^{38}	3×10^{-8}
NGC 4457	SAB(s)0/a	10.7 (4)	6.9	L2	1.0×10^{39}	3.0×10^{40}	3×10^{-5}
NGC 4494	E1-2	15.8 (2)	7.6	L2	9.2×10^{38}	2.8×10^{40}	6×10^{-6}
NGC 4548	SBb(rs)	15.0 (3)	7.6	L2	5.4×10^{39}	1.6×10^{41}	3×10^{-5}

Notes. [d]The mass estimate for NGC 266 is subject to a large uncertainty ($\approx$1 dex) since it is based on using the Fundamental Plane of Merloni et al. (2003) (see the text).

Table B2. Model parameters resulting from the sparsely sampled SED fits. For all models listed below, $R_o = 10^4$, $s = 0.3$ and $i = 30°$.

Galaxy	Model	$\dot{m}_o$	δ	$\dot{m}_{jet}$	p	ϵ_e	ϵ_B	P_{jet}^{mod}	P_{jet}^{obs}	$\dot{m}_{Bondi}$	Refs. and notes
NGC 0266	AD	5.5×10^{-3}	0.3	5×10^{-6}	2.5	0.1	0.01	1.1×10^{42}	–	–	–
NGC 1553	AD	2.5×10^{-3}	0.3	7×10^{-7}	2.5	0.1	0.08	3.7×10^{41}	–	–	–
NGC 2681	JD	–	–	5×10^{-7}	2.1	0.2	0.1	4.3×10^{40}	1.4×10^{41}	–	a
NGC 2681	AD	7.5×10^{-3}	0.01	10^{-7}	2.5	0.1	0.1	8.7×10^{39}	–	–	–
NGC 3169	JD	–	–	3×10^{-5}	2.8	0.99	1.5×10^{-7}	1.3×10^{43}	10^{42}	–	a
NGC 3169	AD	0.03	0.01	2.5×10^{-6}	2.2	0.01	0.01	10^{42}	–	–	–
NGC 3226	JD	–	–	10^{-6}	2.2	0.5	2×10^{-3}	8.7×10^{41}	1.1×10^{42}	–	a
NGC 3226	AD	0.12	0.01	5×10^{-7}	2.3	0.1	0.01	4.3×10^{41}	–	–	–
NGC 3379	JD	–	–	2×10^{-9}	2.05	0.2	0.15	2.1×10^{39}	–	1.6×10^{-5}	1
NGC 3379	AD	6.5×10^{-4}	0.01	–	–	–	–	–	–	–	–
NGC 4457	JD	–	–	1.1×10^{-6}	2.01	0.3	0.01	6×10^{40}	$<4 \times 10^{41}$	–	a
NGC 4457	AD	2.2×10^{-3}	0.1	4×10^{-7}	2.5	0.05	0.01	2×10^{40}	–	–	–
NGC 4494	JD	–	–	10^{-6}	2.01	0.6	0.001	2.3×10^{41}	$<1.4 \times 10^{41}$	–	–
NGC 4494	AD	6.5×10^{-3}	0.01	10^{-7}	2.3	0.1	0.01	2.3×10^{40}	–	–	–
NGC 4548	JD	–	–	1.5×10^{-6}	2.2	0.1	0.01	3.4×10^{41}	4.2×10^{41}	–	a
NGC 4548	AD	8×10^{-3}	0.01	5×10^{-7}	2.5	0.1	0.01	1.1×10^{41}	–	–	–

Notes. (a) Observed jet power estimated using the radio data and the Merloni & Heinz (2007) correlation.
Reference: 1. David et al. 2005.

This paper has been typeset from a TEX/LATEX file prepared by the author.